IEEE Access, Vol. 13, pp. 23072 - 23090, January 2025

Sealless Production Ultracentrifuge and its Magnetically Self-Bearing Openable Motors for Purification in Viral Nanotechnology

E. Hubmann,
D. Steinert,
T. Nussbaumer,
J. W. Kolar

IEEE Access
Multidisciplinary | Rapid Review | Open Access Journal

Received 4 January 2025, accepted 21 January 2025, date of publication 30 January 2025, date of current version 5 February 2025.

Digital Object Identifier 10.1109/ACCESS.2025.3537559

RESEARCH ARTICLE

Sealless Production Ultracentrifuge and Its Magnetically Self-Bearing Openable Motors for Purification in Viral Nanotechnology

EMANUEL J. HUBMANN[1], DANIEL STEINERT[2], THOMAS NUSSBAUMER[2], AND JOHANN W. KOLAR[1], (Life Fellow, IEEE)

[1]Power Electronic Systems Laboratory, ETH Zürich, 8092 Zürich, Switzerland
[2]Levitronix GmbH, 8048 Zürich, Switzerland

Corresponding author: Emanuel J. Hubmann (hubmann@lem.ee.ethz.ch)

This work was supported in part by the Swiss Innovation Agency Innosuisse, and in part by Levitronix GmbH.

ABSTRACT Viral nanotechnology enables new possibilities for gene therapies and vaccines. However, the manufacturing of viral vectors lacks a satisfactory production capable method for purification of full capsids. Empty or partially empty capsids need to be removed to avoid immunotoxicity. The state of the art production ultracentrifuges (PUCFs) are limited, especially in rotational speed to approximately 40 krpm by rotary seals, by complexity and virus containment. This prevents PUCFs from widespread use in industry for viral vector production. This article proposes a novel PUCF type with rotational speed potential towards 100 krpm with a hermetically enclosed process chamber without any rotary seals, i.e. a sealless production ultracentrifuge (SL-PUCF) omitting contamination risk. The openable vertical axis self-bearing motors, the novel sealless flow path design and the needed ultra high-speed potential towards 100 krpm pose new technical problems, for which this article proposes and experimentally validates solutions. A SL-PUCF prototype with its vertical axis magnetically self-bearing openable motors (O-SBMs) and openable burst armor (O-BA) is realized, validated and operated as a system. The general working principle of the SL-PUCF system is experimentally validated by whey protein sedimentation. Furthermore, new future smart capability potential of the proposed new SL-PUCF technology suspended and driven by O-SBMs is unveiled as an outlook and examples shown in case studies.

INDEX TERMS Self-bearing motors, magnetic bearings, openable motors, high-speed motors, thermal management, mechatronic system, viral nanotechnology, production ultracentrifuge.

I. INTRODUCTION

This article presents a novel sealless production ultracentrifuge (SL-PUCF) concept and prototype with a fast exchangeable rotor for viral nanotechnology, shown in Fig. 1. It solves newly identified key problems of the state of the art PUCFs, preventing them currently from broad industry usage in viral nanotechnology. The novel SL-PUCF enables a novel hermetically enclosed sealless vertical axis SL-PUCF rotor, because it is driven and suspended by novel openable magnetically self-bearing motors (O-SBMs) and shielded by a novel openable burst armor (O-BA). This omits contamination risk due to rotary seals. This article is a continuation of the research efforts of [1], where to the knowledge of the authors for the first time, the principle of O-SBMS was experimentally demonstrated. In the following, the gap in the state of the art is identified.

Viral nanotechnology enables new vaccines [2], [3] and gene therapies for previously incurable genetic diseases [4]. Gene transfer via viral vectors is one possible approach, which is considered in this article. The viral vector production process simplified from [5] is as follows: After cell cultivation for viral vectors, the so-called downstream process follows. In the downstream process, the viruses are harvested from the supernatant of the cell culture and from the cells themselves by cell lysis. In the subsequent clarification, producer cells

The associate editor coordinating the review of this manuscript and approving it for publication was Qinfen Lu.

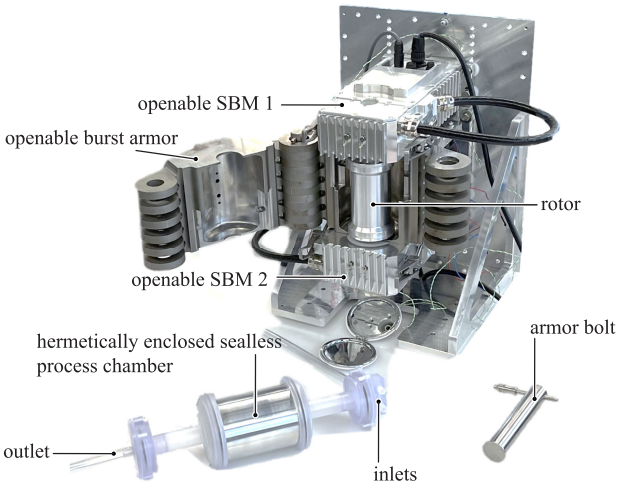

FIGURE 1. Realized system prototype of a novel lab-scale sealless production ultracentrifuge (SL-PUCF). Two openable self-bearing motors (O-SBMs) suspend and drive the vertical axis SL-PUCF rotor. The O-SBMs and an openable burst armor (O-BA) allow for fast exchange of the hermetically enclosed SL-PUCF process chamber including the rotor.

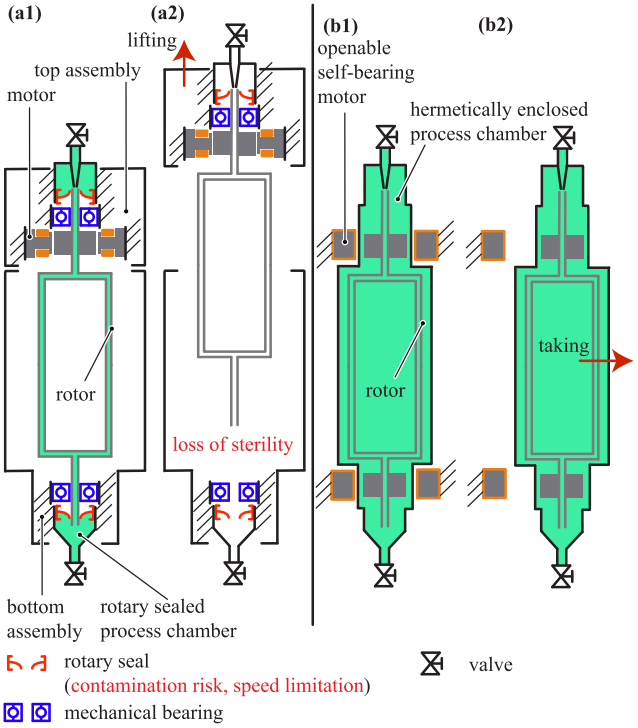

FIGURE 2. (a1) Schematic illustration of a state of the art PUCF. (a2) Replacement procedure of the rotor, causing the loss of the contamination barrier and thus sterility. (b1) Proposed SL-PUCF concept providing a hermetically enclosed process chamber, by replacing rotary seals and mechanical bearings by two O-SBMs. (b2) Process chamber replacement with O-SBMs by simply taking it out of the opened O-SBMs.

and cell debris are eliminated. This is followed by concentration steps that reduce the equipment size required for further processing. During subsequent purification, contaminants are removed as good as possible. In the next polishing steps, impurities and very closely related species are removed as far as possible. Formulation, sterile filtration, fill and finish conclude the production process.

Remaining impurities and very closely related species lead to unnecessary immune reaction [5], negatively affecting the therapy. For viral vector production, extremely high degrees of purity therefore have to be achieved. For this reason, purification is an absolutely critical production step.

In laboratory scale intended for research (LaS-R), it is state of the art to use laboratory scale research centrifuges (LaS-RCF) for clarification and concentration, and laboratory scale research ultracentrifuges (LaS-RUCF) for purification and polishing with excellent results [5]. However, RUCFs are not suited for up-scaling of a biopharmaceutical production process, as everything is tailored to small limited discrete process volumes.

Fig. 2(a1) shows a schematic illustration of a typical state of the art PUCF. Mechanical bearings suspend the rotor, and rotary seals aim to maintain the process chamber contamination barrier during the process. An electric motor in the top assembly drives the rotor. To replace the rotor, it is lifted with the top assembly, causing the loss of the contamination barrier, and thus sterility, as shown in Fig. 2(a2). The proposed SL-PUCF concept of this article is illustrated in Fig. 2(b1), providing a hermetically enclosed process chamber by replacing rotary seals and mechanical bearings by two O-SBMs. The capability of the O-SBMs, to radially open and give way to insert or remove the whole process chamber including the rotor contained inside, allows for exchanging the rotor after a batch without loss of the contamination barrier, as shown in Fig. 2(b2).

An overview of the current state of the art PUCFs is presented in Tab. 1. The current state of the art offers PUCFs in the lab- (LaS-PUCF), pilot- (PiS-PUCF), and production scale (PrS-PUCF) for stepwise up-scaling of the industrial biopharmaceutic production process. The number of PUCF manufacturers and PUCF products is very limited. Partially, the commercial products are based on many decades old technology. Mostly mechanical bearings are employed, requiring the application of rotary seals between rotor and housing. A new effort towards application of contact free magnetic for PUCFs is reported for nano-particles in [8], however its stators cannot open radially to release the rotor. The system needs to be disassembled axially to remove the rotor, resulting in a loss of the contamination barrier, which would be a problem in applying it for biopharmaceutical applications. The rotors for biopharmaceutical PUCFs are in contrast to [8] oriented vertically. The relative centrifugal acceleration of state of the art PUCFs is limited around $C_{\max} = 120'000\,\mathrm{g}$.

In Tab. 2, a summary of limitations and disadvantages of the state of the art PUCFs is given. Such limitations prevent their widespread use in viral vector production. The problems from the application perspective are unveiled in Tab. 2(A) and the technical reasons identified in Tab. 2(B). The scale

TABLE 1. Production Ultracentrifuges (PUCFs): state of the art, and design specifications of the presented prototype of this article.

Scale	Company / *Publication*	Product	Year	Bearing	Axis	$d_{\mathrm{fl,a}}$ [mm]	$\Omega_{\max}$[rpm]	$C_{\max}$[g]	V[mL]	Applications
LaS-PUCF	Alfa Wassermann	Promatix 1000 [6]	2006	mech.	v	*132	35000	90500	55-230	viruses, VLP, VV
PiS-PUCF	Alfa Wassermann	PKII [6]	(-)	mech.	v	130	40500	121000	-4000	viruses, VLP, VV
PrS-PUCF	Alfa Wassermann	KII [6]	1975	mech.	v	130	40500	121000	-8400	viruses, VLP, VV
PiS-PUCF	Thermo Fisher Scientific	Sorvall CC40SNX	(-)	mech.	v	132	40000	118000	1600	viruses, proteins
PrS-PUCF	Thermo Fisher Scientific	Sorvall CC40NX	(-)	mech.	v	132	40000	98000	8000	viruses, proteins
LaS-PUCF	CEPA	Z11	2014	mech.	v	*49	54000	80000	250	nano-LDH [7]
LaS-PUCF	*Konrath et. al, CEPA, EAAT*	*Research Prototype*	2016	DSBM	h	43	app. 64500	100000	270	nano-particles [8]
LaS-PUCF	*Hubmann et. al (this article)*	*Research Prototype*	2024	O-DSBM	v	40	100000	223500	100	viral vectors (VV)

*x: calculated quantity, (-): no information available, mech.: mechanical, v: vertical, h: horizontal.
LaS: lab scale, PiS: pilot scale, PrS: production scale, $d_{\mathrm{fl,a}}$: outer fluid diameter in rotor, $C_{\max}$: maximal centrifugal acceleration, V: rotor volume, VLP: virus like particle, VV: viral vector

TABLE 2. (A) Limitations of state of the art PUCF products for viral vector production, suspected by literature and the authors to be the cause to prevent them from broader usage. (B) Technical reasons and (C) newly defined system level requirements for the novel proposed SL-PUCF concept.

(A) State of the art: problems from an application perspective	(B) Technical reasons	(C) Newly defined technical system level requirements
(1) non-zero risk for infectious virus containing aerosols [5], [9]	rotary seals as weak points of contamination barrier	hermetic virus containment (no seals)
(2) complex rotor insertion and removal	mechanical bearings, lubrication, vibration dampers, crane for rotor removal	radially openable magnetically self-bearing motors (O-SBMs) and burst armor allowing for hermetically contained rotor unit exchange
(3) complex cleaning in place (CIP)	system complexity	rotor removable while hermetically contained
(4) non-zero contamination risk from outside	rotary seals as weak points in contamination barrier	pre-sterilized, hermetically enclosed units can be exchanged
(5) long processing times [5]	rotary seals limit rotational speed	no seals, no mechanical bearings
(6) very limited number of production-scale systems [5] (Alfa Wassermann K-types, Thermo Fischer Scientific Sorvall CC40NX series)	presumption: system complexity	lower complexity, smaller entry hurdle

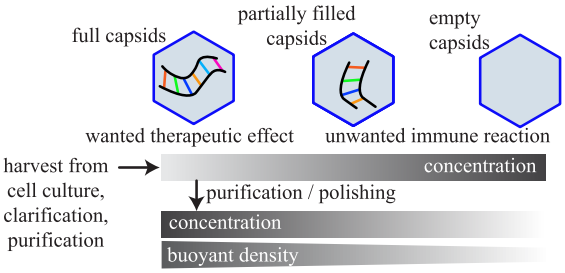

FIGURE 3. In cell cultures for viral vectors, not only the wanted full capsids are produced, which have the intended therapeutic effect. Also empty or partially filled capsids are produced, which only lead to unwanted immune reaction. The same outer properties make it difficult for chromatography to remove the unwanted capsids. The difference in buoyant density enables ultracentrifuges to take over this task, but a scalable widely accepted solution for production scale is missing.

up from LaS-RUCF to PrS-PUCF poses therefore unsolved problems. PrS-PUCFs are thus rarely used in the production scale.

Currently, for production scale production of viral vectors in industry, centrifugation for clarification is replaced by ultrafiltration, while ultracentrifugation for purification is replaced by chromatography and membrane filtration [5] due to the drawbacks listed in Tab. 2(A).

Chromatography in short works based on the outer surface properties of the particles. This implies, that chromatography shows difficulties in separating particles, which have the same or very similar outer surface characteristics.

During the cell-cultivation of viral vectors, only $< 30\%$ of the capsids contain the therapeutic gene of interest, while $> 70\%$ represent empty capsids and $< 10\%$ are only partially filled [10] as conceptually illustrated in Fig. 3. Unwanted co-produced empty or partially empty capsids show the same outer characteristics as full capsids. They do not contribute to the intended therapy, but trigger unwanted unnecessary immune reaction by immunotoxicity in the patient [5], [10].

According to [5], chromatography shows difficulties to separate full from partially or empty capsids. This failure to remove empty or partially empty capsids leads to an unwanted immune response in vivo.

However, due to buoyant density difference between full and empty capsids, equilibrium density ultracentrifugation can separate them. This is shown successfully with LaS-RUCFs [5], [11]. This shows today's dilemma in viral vector purification: great success is achieved in LaS-RUCF, but problems remain in PrS-PUCF. Reference [5] suggests therefore, to apply ultracentrifugation as a polishing step after chromatography for the removal of closely related contaminating species.

Reference [12] states: "there is a lack of an effective and reproducible platform method for the separation of full capsids from the empty capsids"; [11] regards it as part of the "challenges in downstream purification of gene therapy viral vectors". The principle advantage over chromatography by ultracentrifugation, to be able to separate full and empty capsids by buoyant density, leads to new research activity for PrS-PUCF [13]. But the problems of ultracentrifugation unveiled in Tab. 2(A) remain unsolved.

For the earlier process step of clarification, the landscape of available commercial PrS centrifuges to reduce filter area is broad; with for example the CARR Biosystems UniFuge and sartorius stedim Ksep and additionally with very new developments: Alfa Laval CultureOne [14] and GEA kytero [15].

However, for ultracentrifugation, today no solution exists, which omits the problems in Tab. 2(A) and solves the technical reasons in Tab. 2(B). Based on these identified problems, to overcome them, new system level requirements are defined in Tab. 2(C).

The main objective of this study therefore is to find technical solutions to close today's technology gaps for realizing a SL-PUCF prototype for viral nanotechnology and to provide a first system validation thereof with an outlook on its unique future capability potential.

The proposed and realized SL-PUCF concept in this article is presented in Fig. 4. The concepts realized O-SBM hardware is shown in Fig. 4(a), allowing to radially open due to the splitting plane, separating the O-SBM halves O-SBM 1a and O-SBM 1b. This enables the placement of a hermetically sealed process chamber shown in Fig. 4(b). Feed suspension and density gradient media can be fed from above via the inlets. A further connector enables the supply and removal of the process gas surrounding the rotor. During the ultracentrifugation process, the fed particles separate along the density gradient in radial direction and settle at the radius of their corresponding density. An outlet allows the separated particles to be discharged.

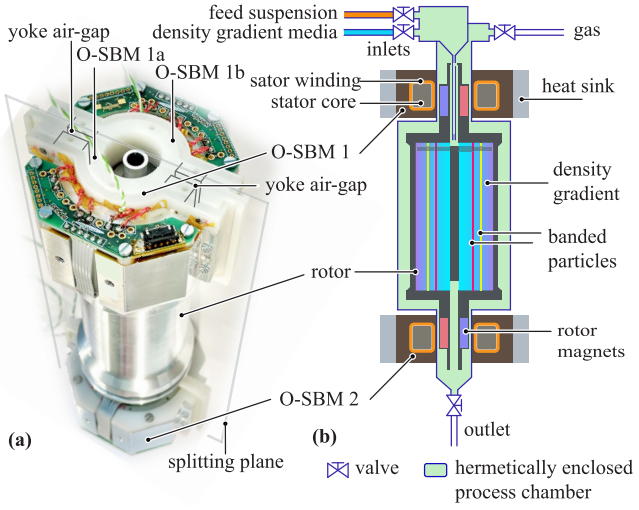

FIGURE 4. (a) Sealless production ultracentrifuge drive system prototype consisting of two along the splitting plane openable self-bearing motors (O-SBM 1 and O-SBM 2). (b) Schematic section view of the proposed sealless production ultracentrifuge concept.

In the following, component level requirements RY, which currently show technology gaps Pi, are identified. They have to be overcome to fulfill the system level requirements defined in Tab. 2(C). The SL-PUCF system is divided into the three main SL-PUCF hardware components Cj: the O-SBMs, C1, the SL-PUCF rotor, C2, and the burst armor, C3, as shown in Fig. 5.

For C1, O-SBMs were experimentally studied and proven to work for the first time in [1], to the author's knowledge. A solid test-rotor was magnetically levitated and accelerated to a rotational speed of up to 103 krpm with a horizontal axis of rotation.

For the O-SBMs, the first component requirement RA with problems is identified as the need for yoke air-gaps (y-AGs) between the stator halves due to corrosion protection enclosing or coating of the stator yokes in the splitting plane. This combined with compared to [1] newly required vertical rotor axis leads to the new problems P1, the axial stiffness ripple $\Delta k_{\mathrm{B,ax}}$, and P2, the excitation of an axial rotor displacement $z\prime$. As solutions S1 and S2, a yoke design feature and rotor magnet design guidelines are proposed.

The problem of yoke air-gap induced parasitic currents was solved in [1] with a feed-forward current control scheme and is mentioned here for completeness.

In biopharmaceutical clean-rooms, passive cooling is preferred over active cooling to not disrupt the controlled airflow in the room. It furthermore omits contamination risk by cooling liquid and reduces complexity, especially for the openable part of the O-SBMs. However, this is currently prevented by the problem P3, that the heat extraction from the O-SBM windings at such high rotational frequencies with an aluminum heatsink generates too high eddy current losses, and non-conductive potting material results in too high winding temperature. Therefore, a new passive heat extraction solution S3, which is scalable from LaS-PUCF to PrS-PUCF is required. The solutions S1-S3 for the problems P1-P3 for the component C1, the O-SBMs, are presented in Sec.II.

For the component C2, the SL-PUCF rotor, the requirement RC of a sealless fluid path leads to the problem P4, that no seals are available anymore to guide the fluid. As a solution S4, a new internal SL-PUCF rotor topology for guiding the fluid without any rotary seals is proposed. Additionally the absence of rotary seals leads to the problem P5, that dynamic filling during rotation of the rotor is required, where rotor suspension stability becomes an issue. As solutions, a novel inflow distributor S5a, and novel equalizing channels S5b are proposed. The solutions S4-S5b for the component C2, the SL-PUCF rotor, are presented in Sec.III.

The SL-PUCF needs a burst armor, the component C3, to contain rotor fragments in case of a rotor failure. The system requirement of a fast exchangeable rotor and process chamber leads to the component requirement RD of an openable burst armor. The problem P6 arises to contain the high rotational energy despite the potential weak points of the joints. As solution S6, a novel burst armor design is proposed, tailored to contain the high rotational energy while capable to open for rotor exchange, presented in Sec.IV.

Fig. 5 shows additionally the interconnection of SL-PUCF components and its design domains including electric, magnetic, thermal, mechanic and fluiddynamic domains,

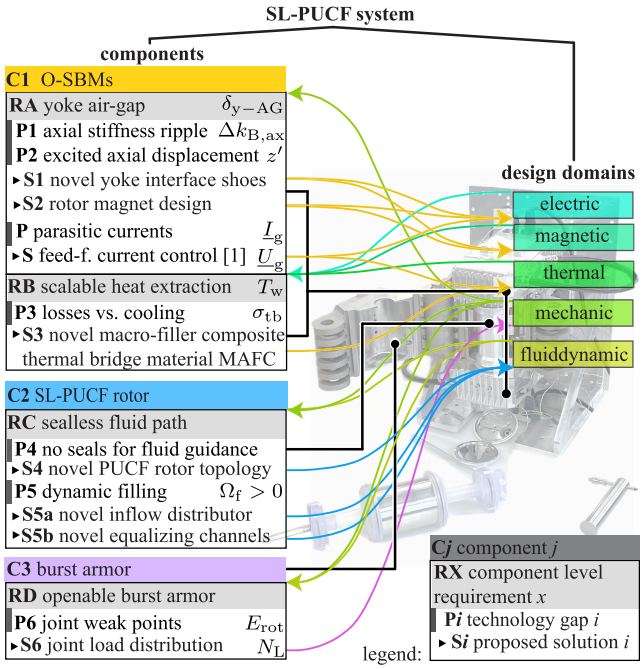

FIGURE 5. For each of the SL-PUCF components, O-SBMs C1, the SL-PUCF rotor C2, and the burst armor C3, identified problems P*i* and solutions S*i* thereof. Additionally, the interdisciplinary interrelations to the design domains are shown.

highlighting the interdisciplinary nature of the SL-PUCF system.

Sec.V shows an experimental system validation of the working principle of the proposed novel SL-PUCF concept with a realized LaS-PUCF prototype. Sec.VI gives an outlook to the novel future smart capability potential of the SL-PUCF, which is newly possible thanks to the O-SBMs as a drive system. Examples for applications of such capabilities are shown additionally in the form of three case studies. In Sec.VII, a brief discussion of the findings is given. Sec.VIII summarizes the findings.

II. COMPONENT C1: OPENABLE SELF-BEARING MOTORS

A. TECHNOLOGY GAPS DUE TO COMPONENT REQUIREMENT RA; YOKE AIR-GAPS

To enable the SL-PUCF rotor, shown in Fig. 4, to be emptied at the end of the ultracentrifugation process cycle, or for continuous flow processing, the axis of rotation must be vertical. Until now, O-SBMs have only been operated with a horizontal axis of rotation when introduced in [1], as illustrated in Fig. 6(a). In horizontal operation, the axial passive magnetic reluctance forces $F_{ax,i}$ are in equilibrium, if both rotor magnets are magnetized in the same radial direction (no angular offset), i.e. aligned.

1) PROBLEM P1: AXIAL STIFFNESS RIPPLE

The new vertical rotor operation with O-SBM, as illustrated in Fig. 6(b), leads to axially unbalanced $F_{ax,i}$. They are unbalanced due to the weight force F_G of the rotor mass m_{rot}, which needs to be compensated by $F_{ax,i}$. As shown in the following, O-SBMs exhibit a parasitic axial stiffness ripple $\Delta k_{B,ax}$. The combined stiffness ripple is for a vertical axis of rotation unbalanced, whereas its components cancel each other out with a horizontal axis of rotation and aligned magnet orientation.

The passive axial magnetic bearing stiffness $k_{B,ax,i}$ together with m_{rot} lead to a spring-mass system with an axial resonance frequency $\omega_{res,ax}$ as illustrated in Fig. 6(c).

Overcoming this resonance was not a problem for the O-SBMs in [1], because they were operated with horizontal axis of rotation with resulting cancellation of $F_{ax,i}(\varphi)$. However, this is not the case for vertical axis rotor operation as studied in this article. In this case, $k_{B,ax,i}$ excite the axial resonance mode and axial displacement (problem P2), which makes it difficult or impossible to pass through the axial resonance. A state of the art solution for magnetic bearings would be, to install additionally an active axial magnetic bearing. However, this would significantly increase the complexity of both the O-SBM stator and rotor. Additionally, from a process perspective, it would take away system design freedom for the SL-PUCF flowpath design in the rotor. For this reason, the mechanisms of the axial excitation are investigated in depth, and the corresponding negative effects are reduced by design measures to enable safe passing through $\omega_{res,ax}$.

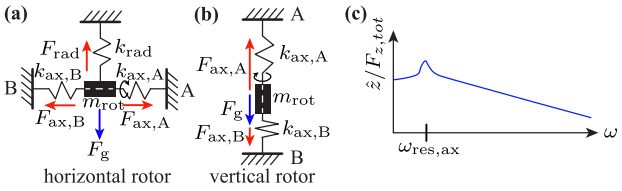

FIGURE 6. (a) Balanced axial rotor forces $F_{ax,i}$ in horizontal rotor axis operation. (b) Vertical rotor axis orientation leads to unbalanced axial rotor forces and therefore to axial excitation by non canceling axial stiffness ripples. (c) The passive magnetic axial resonance frequency $\omega_{res,ax}$.

2) SOLUTION S1: NOVEL YOKE INTERFACE SHOES TO COUNTERACT YOKE AIR-GAP INDUCED AXIAL STIFFNESS RIPPLE

The y-AGs between the stator halves lead to a dependency of the magnetic circuit reluctance on the rotor angle φ.

The question remains, why very small y-AGs of only 0.2 mm as in this articles prototype lead to a significant adverse effect. This is investigated first. Fig. 7(a) shows a cross-section of an O-SBM. It shows the cross-sectional areas through which half of the rotor permanent magnet (PM) flux $\phi_d/2$ has to pass. The y-AG length is much smaller than the total air-gap of the magnetic circuit. However, the y-AG surface is much smaller compared to the air-gap surface shown in Fig. 7(a). This cross-section area difference explains the surprising substantial influence of the y-AGs.

TABLE 3. Solution S1: yoke interface shoes - main result.

S1: problem remedy	main results
axial stiffness ripple $\Delta k_{\mathrm{B,ax}}$ RMS reduction for a yoke air-gap of 0.2 mm and a yoke air-gap surface increase of 33%	−39%

Fig. 7(b1) shows the stator yoke prototype made of soft magnetic composite (SMC) material from [1]. It is generally not possible to manufacture sharp edges out of SMC due to its brittleness. There will always be a small radius, which further reduces the y-AG cross-sectional area. For small motors, the problem of the y-AG becomes therefore even more acute.

With the aim of reducing the parasitic effects of the y-AGs, the solution S1 is proposed in this article and realized as a prototype: novel yoke interface shoes. The intention is to increase the y-AG surface by widening of the yoke cross-section at the interface as shown in Fig. 7(b2).

Fig. 7(c) shows magnetostatic 3D-FEM results of the magnetic flux density B distributions in a O-SBM cross-section with the novel yoke interface shoe. Two distinct angular rotor positions are shown. In the first, the d-axis is perpendicular to the stator splitting plane. Half of the rotor flux $\phi_{\mathrm{d}}/2$ has to cross each y-AG, as shown in Fig. 7(c1). The rotor flux utilizes the full widening of the yoke at the novel interface shoes, supporting the theory in Fig. 7(a). It crosses the widened y-AG surface without substantial fringing flux, in Fig. 7(c2). This supports the theory in Fig. 7(a) as well, as apparently half of the rotor flux must indeed pass through the y-AG.

In the second case the d-axis lies in the splitting plane as shown in Fig. 7(c4). In this case, no rotor flux passes through the y-AG, but enters the yoke through the surfaces facing the rotor as shown in Fig. 7(c3). This case therefore does not lead to an increase in reluctance. The reluctance of the magnetic circuit varies during rotor rotation between these cases.

Fig. 7(d) unveils the occurring torque ripple for y-AGs lengths of $\delta_{\mathrm{y}} = 0.2\,\mathrm{mm}$ and $\delta_{\mathrm{y}} = 0.4\,\mathrm{mm}$ determined with 3D-FEM. The increase of the torque ripple when doubling the y-AG proves it to be the cause. The new stator yoke with the novel yoke interface shoes shows a reduction in torque ripple of 21 % for $\delta_{\mathrm{y}} = 0.2\,\mathrm{mm}$ and 20 % for $\delta_{\mathrm{y}} = 0.4\,\mathrm{mm}$ for an increase of the y-AG cross-sectional area by 33 %. Fig. 7(e) shows the axial stiffness ripple $\Delta k_{\mathrm{B,ax}}$ resulting from the y-AGs. However, the new yoke interface shoes allow a RMS reduction of $\Delta k_{\mathrm{B,ax}}$ by 39 % for $\delta_{\mathrm{y}} = 0.2\,\mathrm{mm}$ and 27 % for $\delta_{\mathrm{y}} = 0.4\,\mathrm{mm}$. Tab. 3 summarizes the main findings of solution S1.

3) PROBLEM P2: EXCITED AXIAL DISPLACEMENT

An axial displacement z of the rotor leads to an axial restoring force F_{z} in the stator as shown in Fig. 8(a), defined by the axial stiffness k. The combination of two O-SBMs with a common rotor leads to a superposition of these axial forces shown in Fig. 8(b). The combined stiffness k_{tot} depends on the

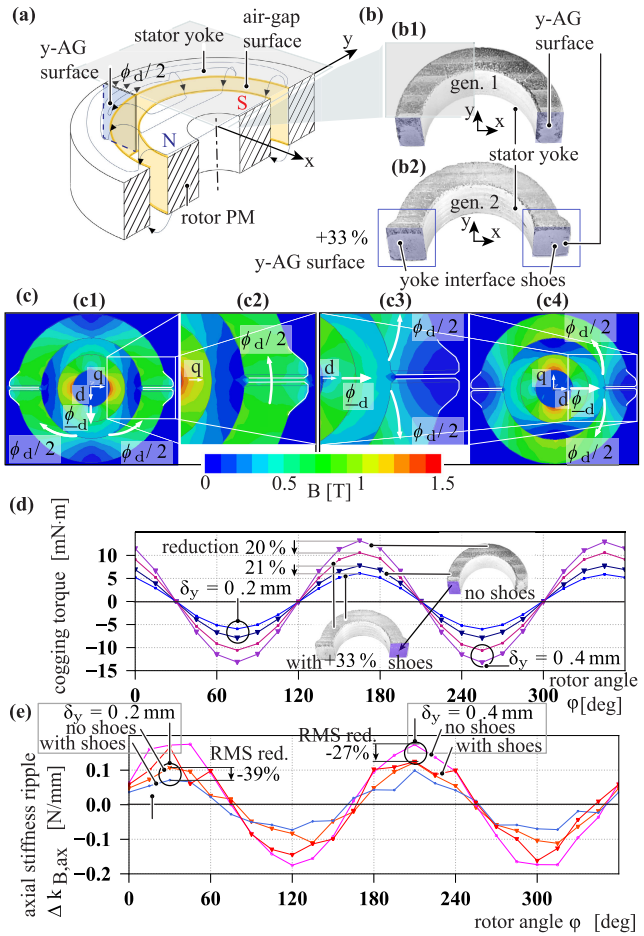

FIGURE 7. (a) Cross-section through a O-SBM. The yoke air-gap (y-AG) surface is by factors smaller than the air-gap surface. (b) Realized stator yokes, (b1) first generation openable stator yoke from [1], (b2) improved second generation version with solution S1: novel yoke interface shoes. (c) Magnetostatic 3D-FEM result of the flux density distribution for the novel yoke interface shoes. (d) Yoke interface shoes lower the y-AG induced torque ripple and (e) the axial stiffness ripple substantially.

rotor angle φ and the relative magnetization direction offset of the two rotor magnets θ as shown in Fig. 8(c). Based on the 3D-FEM simulation results of Fig. 7(e), the axial stiffness k is modeled as a mean value with a superimposed second harmonic caused by the y-AGs:

$$k_{\mathrm{A}} = k_{\mathrm{ax}} + k_{\Delta} \sin(2\varphi + \theta) \tag{1}$$

$$k_{\mathrm{B}} = k_{\mathrm{ax}} + k_{\Delta} \sin(2\varphi)\,. \tag{2}$$

The rotor displacement in relation to the magnetic center of the rotor is designated by the new coordinate z'. A pre-set offset of the rotor magnets w.r.t. the stators is referred to here as z_{ps}. Fig. 8(c) shows the combined axial force generation by both O-SBMs, it results as:

$$F_{\mathrm{z,tot}}(z') = (z' + z_{\mathrm{ps}}) \cdot k_{\mathrm{B}}(\varphi, \theta) + (z' - z_{\mathrm{ps}}) \cdot k_{\mathrm{A}}(\varphi, \theta)\,. \tag{3}$$

The averaged rotor displacement in axial direction $\bar{z'}$ is determined by the balance of the gravitational force F_{g} on

the rotor mass m_{rot} with the two superimposed averaged axial stiffnesses $\bar{k}_{\mathrm{ax}}$:

$$\bar{z'} = -\frac{m_{\mathrm{rot}} \cdot g}{2\bar{k}_{\mathrm{ax}}}. \tag{4}$$

This averaged value turns out to be independent of z_{ps}. The assumption here is, that the axial load capacity limit of the O-SBMs has not yet been exceeded. The axial equation of motion for the rotor is

$$F_{\mathrm{z,tot}}(z') = -m_{\mathrm{rot}} \cdot g + m_{\mathrm{rot}} \cdot \ddot{z'}. \tag{5}$$

It shows a resonance frequency of

$$f_{\mathrm{res,ax}} = \frac{1}{2\pi} \cdot \sqrt{\frac{2 \cdot k_{\mathrm{ax}}}{m_{\mathrm{rotor}}}}. \tag{6}$$

For high frequencies, i.e. speeds far above f_{res}, the system acts as a low-pass filter and axial vibrations are damped. Therefore, for passing through $f_{\mathrm{res,ax}}$, the low frequencies are relevant. The quasi-static axial rotor displacements are analyzed for this purpose. The quasi-static force equilibrium is as follows:

$$F_{\mathrm{z,tot}}(z') = -m_{\mathrm{rot}} \cdot g. \tag{7}$$

Solved for the axial rotor displacement z', the result is:

$$z' = \frac{-m_{\mathrm{rot}} \cdot g - z_{\mathrm{ps}} \cdot k_{\Delta} \left[\sin(2\varphi) - \sin(2\varphi + \theta)\right]}{2k + k_{\Delta} \left[\sin(2\varphi) + \sin(2\varphi + \theta)\right]}. \tag{8}$$

The question arises, which relative rotor magnet orientation offset θ should be selected between the two rotor magnets in order to keep the axial vibration levels at low speeds as small as possible. Additionally, the influence of the axial pre-set z_{ps} displacement remains unclear. This is analyzed in the following.

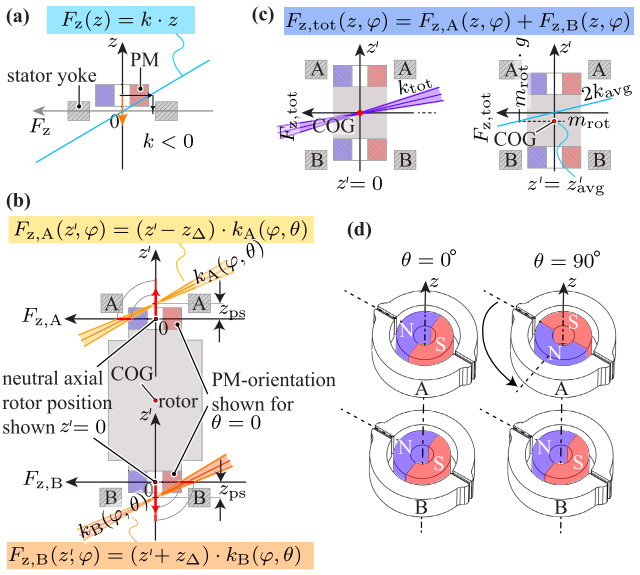

FIGURE 8. (a) Axial bearing stiffness k of a SBM. (b) Individual axial stiffnesses of the two O-SBMs. The rotor is shown with a pre-set offset z_{ps} and axially in neutral symmetric position. The axial stiffnesses k vary during rotation due to the y-AGs. (c) Combined axial stiffnesses of the two SBMs and average combined axial stiffness k_{avg} and rotor position. (d) The two investigated rotor magnetization orientation combinations.

4) SOLUTION S2: MAGNET DESIGN - NOVEL GUIDELINE FOR OPTIMAL CHOICE OF RELATIVE MAGNET ORIENTATION OFFSET θ

The extreme values of the quasi-static axial vibration amplitudes can be determined for the cases $\theta = 0°$ and $\theta = 90°$ considering the value ranges of the sine values in Eq.8:

$$z'_{\theta=0°} = \frac{-m_{\mathrm{rot}} \cdot g}{2 \cdot (k \pm k_{\Delta})} \tag{9}$$

and

$$z'_{\theta=90°} = \frac{-m_{\mathrm{rot}} \cdot g \pm 2\, z_{\mathrm{ps}} k_{\Delta}}{2\, k}. \tag{10}$$

The resulting quasi-static axial vibration amplitudes are:

$$\hat{z'}_{\theta=0°} = \frac{m_{\mathrm{rot}} \cdot g \cdot k_{\Delta}}{2 \cdot \left(k^2 - k_{\Delta}^2\right)} \tag{11}$$

and

$$\hat{z'}_{\theta=90°} = \frac{z_{\mathrm{ps}} k_{\Delta}}{k}. \tag{12}$$

With the introduction of the rotor pre-set axial offset ratio α of the pre-set displacement z_{ps} to the average axial rotor displacement $\bar{z'}$:

$$\alpha := \frac{z_{\mathrm{ps}}}{\bar{z'}} \tag{13}$$

the ratio R of the amplitudes for the two θ values can be determined as

$$R = \frac{\hat{z'}_{\theta=0°}}{\hat{z'}_{\theta=90°}} = \frac{m_{\mathrm{rot}} \cdot g \cdot k}{2 \cdot \left(k^2 - k_{\Delta}^2\right) z_{\mathrm{ps}}} = \frac{1}{\left(1 - \left[\frac{k_{\Delta}}{k}\right]^2\right) \cdot \alpha}. \tag{14}$$

This relationship is shown in Fig. 9. Depending on α and the ratio k_{Δ}/k, it is shown, which θ value leads to the lowest quasi-static vibration amplitudes. Thus, it is analytically derived, which θ value is optimal for a given system. According to these results, there is even a case, in which the quasi-static axial vibrations can be completely eliminated: for the case of $\left(z_{\mathrm{ps}} = 0 \,\&\, \theta = 90°\right)$. In the following, however, it is shown why a system with $z_{\mathrm{ps}} > 0$ has other important advantages. The derived design guideline also shows the optimum magnet orientation for such a system.

5) SOLUTION S2: MAGNET DESIGN - NOVEL GUIDELINE FOR ROTOR MAGNET DIMENSIONS

The design of the rotor magnet has an influence both on the motor performance, as well as the magnetic bearing properties. It is therefore also linked to the axial resonance. Fig. 10(a) shows a to the stator yoke centered magnet whose length l_{m} corresponds to that of the stator yoke, l_{s}.

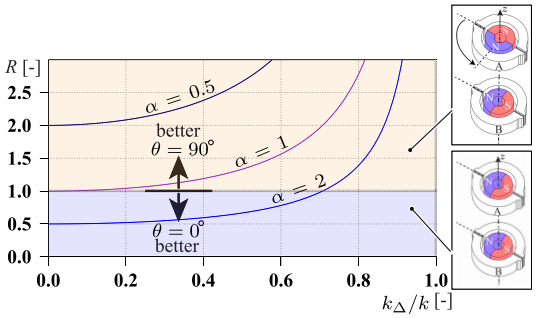

FIGURE 9. Guideline for the optimal magnet orientation offset θ for a vertical axis double O-SBM system based on the axial offset ratio α, and the stiffness variation. R is the ratio of the quasi-static axial vibration amplitudes of $\theta = 90°$ to $\theta = 0°$. $R > 1$ indicates that $\theta = 90°$ is favorable, while for $R < 1$ $\theta = 0°$ is superior.

TABLE 4. Solution S2: rotor magnet design - main result.

S2: problem remedy	main results
counteracting axial displacement excitation	design guideline for relative rotor magnet orientation offset θ, and for the rotor magnet dimensions

Additionally, an illustration of a potential extension of the magnet, that goes beyond this, is shown. A length extension of the magnet leads to additional torque formation by stray field utilization by the toroidal windings of the stator. Fig. 10(b) shows the resulting increase in the torque constant k_t and the resulting axial force F_z as a percentage compared to the values of the reference magnet with $l_m = l_s$. There is a very strong increase in k_t with increasing l_m. For the O-SBMs of this article, the increase in k_t is more than 30% with a magnet extension of 50%. The magnetic center of the magnet shifts relative to the stator by the distance a in Fig. 10(a), which leads to the axial restoring force shown in Fig. 10(b). Fig. 10(c) shows an additional axial shift b of the rotor magnet. The magnet center is therefore axially shifted by $a + b$. Fig. 10(d) shows the resulting reduction of k_t. Over the entire stable range of axial stiffness, k_t is higher than in the centered case $l_m = l_s$. Thus, the presented O-SBM design is within the stability limits beneficially largely insensitive to axial shift or rotor weight induced displacement regarding motor performance.

This good-natured behavior allows a short overall length design of the thin rotor shaft that protrudes from the rotor cylinder l_{rs}, which keeps the rotor bending resonance frequency advantageously low. This also facilitates a sufficiently large axial clearance c_{ax} between the rotor and the centrifuge housing to cross $f_{res,ax}$. Therefore, the prototype of this article is realized with $z_{ps} > 0$, $\alpha > 1$, and $R < 1$. This leads according to Fig. 9 to an optimal magnet orientation angle $\theta = 0°$, which is implemented in the prototype. Tab. 4 summarizes the main findings of solution S2.

B. TECHNOLOGY GAPS FOR COMPONENT REQUIREMENT RB: SCALABLE HEAT EXTRACTION

1) PROBLEM P3: LOSSES VS. COOLING

Very high-speed slotless motors with toroidal windings generate high-frequency stray fields. They therefore do not

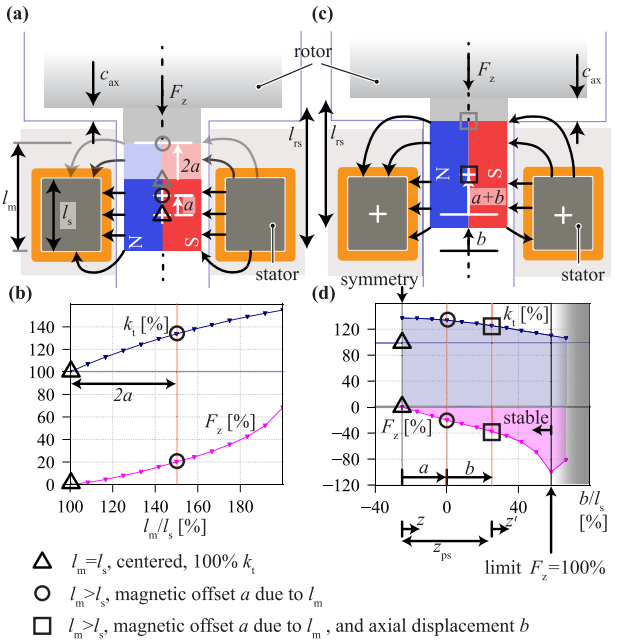

FIGURE 10. (a) Rotor magnet length l_m increase towards the rotor center, exceeding the stator length l_s. (b) Resulting increase in torque constant k_t and non-zero axial reluctance force F_z. (c) Additional axial displacement b with (d) resulting influence on k_t and F_z.

allow close contact direct cooling of the stator via an aluminum heat-sink, as it is usually the case for motors, or only with the acceptance of high additional losses [16], [17], [18]. Therefore, electrically conductive materials in the immediate vicinity of the stator should be avoided.

As a consequence, the heat-sink needs to be placed at distance form the stator. A thermal bridge material is needed to bridge this gap. An ideal thermal bridge material is electrically insulating but highly thermally conductive.

The O-SBMs of this article have a design efficiency η_{O-SBM} of 89.2 %, and a peak continuous shaft power to overcome the rotor gas friction at 100 krpm of 280 W, resulting in to be dissipated motor losses of 33.9 W. For a good potting material with a thermal conductivity of 1.2 W/(mK), the thermal resistance of the thermal bridge of these O-SBMs between winding and heatsink analytically calculated is 2.2 K/W. Therefore, the temperature drop from stator winding to heatsink is 74.6 K. For a heatsink temperature of 40°C, the winding surface temperature becomes 114.6°C. This temperature is too high for the close by position sensing electronics.

This type of motor is therefore currently limited in applicability and scalability for high power outputs. However, the scale up is necessary in the biopharmaceutical industry for the process scale up from LaS systems to PiS and further to PrS systems.

2) SOLUTION S3: NOVEL MACRO-FILLER COMPOSITE (MAFC) THERMAL BRIDGE MATERIAL

As a solution, the disadvantage of the large distance to be bridged thermally is transformed into an advantage. The large

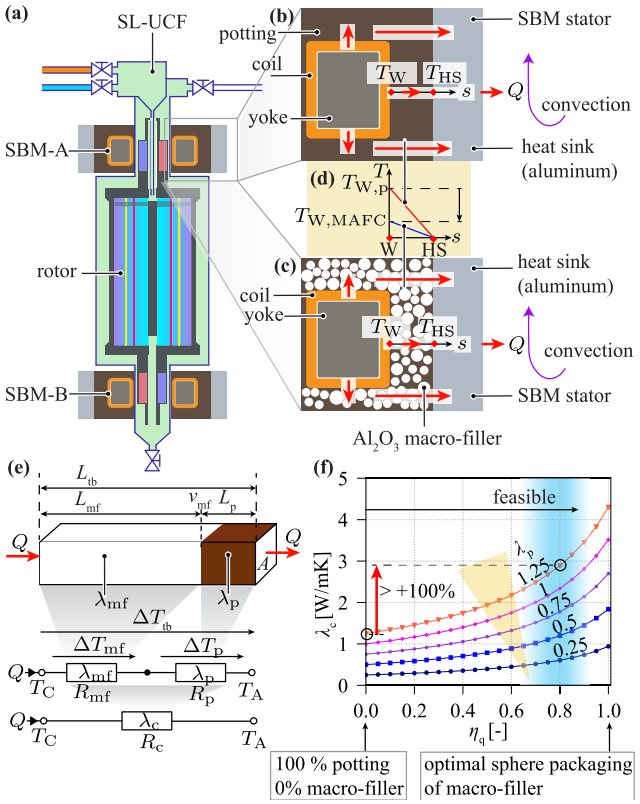

FIGURE 11. (a) SL-PUCF concept with O-SBMs suspending and driving the SL-PUCF rotor. (b) Heat sink at distance to the stator stray fields, with potting material as a thermal bridge. (c) Novel macro-filler composite (MAFC) of macroscopic ceramic (aluminum oxide Al_2O_3) spheres surrounded by potting material, forming a substantially better thermally conductive and electrically insulating thermal bridge material. (d) Conceptually shown thermal bridge material dependent effect on the winding temperature T_W. (e) MAFC thermal resistance conservatively modeled as a series connection of the individual volume share of the two materials. (f) Theoretical lower limit of the achievable MAFC thermal conductivity λ_c based on the filling quality η_q and the thermal conductivity of the potting material λ_p.

distance allows to place few mm large macroscopic filling elements within the potting in the space to be bridged. This is referred to in this article as macro-filler composite (MAFC). The advantage over conventional microscopic fillers is, that the heat can be conducted over comparably long distances via the macro-filler instead of through a microscopic mixture of casting compound and filler particles.

In addition, advantageously the cured hardness is high, which is not the case for soft silicone based potting compounds. Furthermore, MAFC are realizable at a substantially lower material cost compared to special potting compounds with micro-fillers. Moreover, the potting compound retains its low viscosity between the macro-fillers, which means that a good bond can be achieved to the stator winding wires and the heat sink surface. This is more difficult with micro-fillers due to the paste-like consistency of the compound.

The solution S3 proposed in this article is a ceramic macro-filler and epoxy-potting MAFC. Electrically insulating aluminum oxide Al_2O_3 ceramic spheres, which are available on the market in various size classes at very low cost, are proposed as macro-fillers. At 30 W/(mK), they have a thermal conductivity, that is 30 . . . 60 folds higher than that of conventional potting compounds. Al_2O_3 is additionally beneficially electrically insulating. The selected sphere size for this study is $3-7$ mm with costs for small quantities of 30 Euros/kg and for large quantities 16.50 Euros/kg. However, smaller sizes of e.g. $0.75-1.5$ mm are also available. The price for the potting compound ER2074 used in this study is 84 Euros/kg for large quantities. Although custom manufactured ceramic parts would be thermally even better, the MAFC proposed here is an extremely cost effective solution, which flexibly can be used for arbitrary geometries without expensive manufacturing of ceramic parts.

3) SOLUTION S3: THEORETICAL INVESTIGATION OF MAFC

Fig. 11(a) schematically shows the proposed SL-PUCF concept. Fig. 11(b) and (c) show the stator in two versions, both with the aluminum heat-sink placed at a distance. In version (b), the distance between the stator and heat-sink is bridged with conventional potting compound. In the new version (c) below, the novel proposed MAFC is used. Fig. 11(d) shows conceptually the intended reduction in motor winding temperature T_W. Fig. 11(e) shows a series thermal resistance model for the conservative estimation of the thermal conductivity λ_c of MAFC. The series model of MAFC is conservative because it neglects beneficial parallel heat paths which are also present in MAFC, which increase λ_c. The series model is therefore a conservative estimate for a lower limit of λ_c. The actual value of λ_c is thus guaranteed to lie above, while neglecting contact resistances at the material interfaces.

The temperature drop ΔT_{tb} over the thermal bridge is according to the serial model in Fig. 11(e):

$$\Delta T_{tb} = \frac{Q}{A}\left[\frac{L_{tb}}{\lambda_c}\right] = \frac{Q}{A}\left[\frac{v_{mf}\cdot L_{tb}}{\lambda_{mf}} + \frac{(1-v_{mf})\cdot L_{tb}}{\lambda_p}\right], \tag{15}$$

with the heat flux Q, cross-section A, length of the thermal bridge L_{tb}, volume fraction of the macro-filler v_{mf}, thermal conductivities of the macro-filler material λ_{mf} and potting material λ_p. This results in the thermal conductivity λ_c of MAFC:

$$\lambda_c = \frac{\lambda_{mf}\lambda_p}{v_{mf}\cdot(\lambda_p-\lambda_{mf})+\lambda_{mf}}. \tag{16}$$

The mathematically optimal possible packing density of spheres, i.e. volume fraction in 3D, $v_{s,max}$ assuming spheres of the same size is [19]:

$$v_{s,max} = \pi/\sqrt{18} = 0.7404. \tag{17}$$

Based on this theoretical optimum, a MAFC filling quality η_q is defined here, which quantifies the achieved MAFC volume fraction v_{mf} relative to the theoretical optimum $v_{s,max}$.

$$\eta_q = v_{mf}/v_{s,max}. \tag{18}$$

This results in the thermal conductivity of MAFC:

$$\lambda_c = \frac{\lambda_{mf}\lambda_p}{\eta_q \cdot v_{s,max} \cdot (\lambda_p - \lambda_{mf}) + \lambda_{mf}}. \quad (19)$$

Fig. 11(f) shows the lower limit of achievable MAFC thermal conductivity λ_c, depending on the MAFC filling quality η_q. The positive effect of MAFC is amplified, the better the conductivity of the potting material, because the Al_2O_3 macro-filler has substantially higher thermal conductivity then the potting material. For the O-SBMs of the SL-PUCF prototype, the selected potting material for the MAFC is ER2074 with a thermal conductivity of 1.25 W/(mK). With a MAFC filling quality of $\eta_q = 0.6 \ldots 0.8$, an improvement of over 100 % in thermal conductivity from λ_p to λ_c is thus expected based on the series model.

4) SOLUTION S3: MAFC REALIZATION AND THERMAL CONDUCTIVITY MEASUREMENT UNITS

To experimentally validate the model predicted improvement in λ_c compared to λ_p, thermal conductivity measurement units are designed and built. Fig. 12(a) shows their working principle. A heat flux Q is generated by the heating resistor R_i. Its dissipated power Q is measured by the DC current through R_i and voltage across R_i. A square copper heat spreader with 32 mm side length enables a uniformely distributed heat flux due to its higher thermal conductivity compared to potting material by two orders of magnitude ($\lambda_{Cu} = 391$ W/mK). Q is then injected into the medium under test. The heat is conducted to the measurement unit heat sink which is actively cooled by a cooling fan. The temperature difference between the inner surfaces of the heat spreader and the heat sink, $\Delta T = T_c - T_{HS}$, is measured. ΔT is only dependent on Q, the thermal conductivity of the medium under test, and its cross-section. The airflow condition at the measurement unit heat sink therefore has no influence on the measured ΔT. It only changes the absolute temperatures, but not ΔT and is therefore irrelevant for the measurement. In the SL-PUCF system, the heat-sink is comprised of the O-SBM housing including the mounting structure and is dimensioned large enough to ensure a heat sink temperature of not higher than 40° C. The heat sink in the measurement units with the fan is only for the measurement purpose. Fig. 12(b) shows the hardware realization of a thermal conductivity measurement unit. It additionally shows the filling process with Al_2O_3 MAFC spheres. As a MAFC production method, a repeated layering of potting material, placement of a macro-filler layer, and soft compaction with a soft plastic stick was conducted.

Fig. 12(c) and (d) show the four realized thermal conductivity measurement units before, and after filling respectively. Two are filled with MAFC and two with potting only, as a comparison. Fig. 12(e) shows the setup for the thermal conductivity measurement.

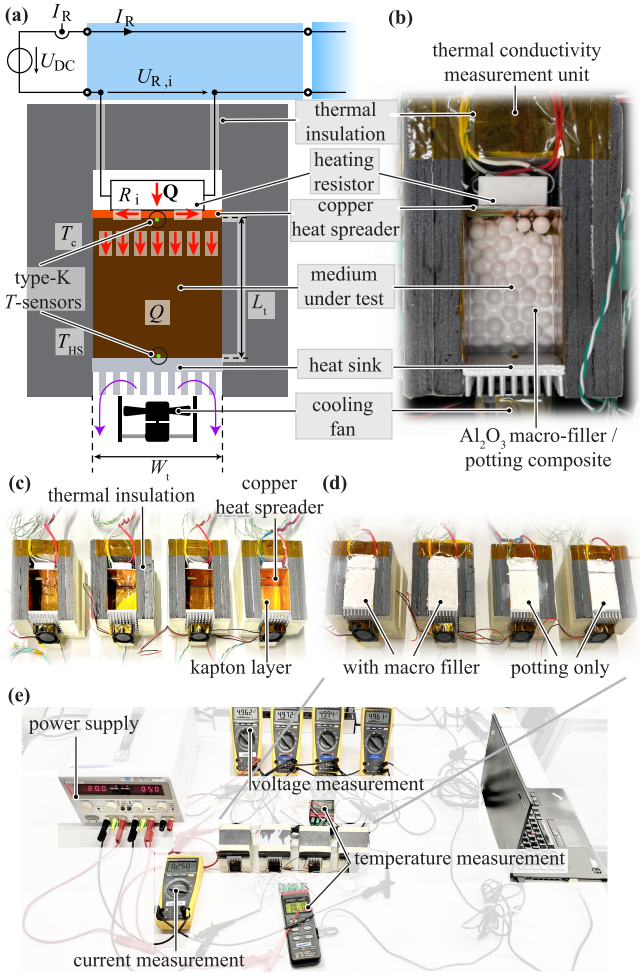

FIGURE 12. (a) Schematic of the working principle of the purpose built measurement units for the measurement of the thermal conductivity of the novel ceramic macro-filler composite (MAFC) thermal bridge material. (b) One out of the four realized measurement units. (c) Measurement units before potting. (d) Potted units before being covered with a thermal insulation lid. (e) Setup for the thermal conductivity measurements.

5) SOLUTION S3: EXPERIMENTAL VALIDATION OF MAFC THERMAL CONDUCTIVITY IMPROVEMENT

Fig. 13(a) shows the measured temperature difference ΔT rises for a power input per measurement unit of $P_R = 1.25$ W. The MAFC performs substantially better than the potting alone. This becomes more evident by computing the resulting thermal conductivity, taking into account the leakage heat flux $Q_{leak,ins}$ through the thermal insulation in the measurement units. $Q_{leak,ins}$ is determined by measuring the outer measurement unit surface temperature with a contact-less infrared thermometer, the thermal conductivity of the polyurethane foam insulation of 0.02 W/(m · K), and the measured internal temperatures. For the λ_c characterization, due to linearity of heat conduction, the specific amount of Q applied and the absolute temperatures T_c and T_{HS} are on its own irrelevant. Only the measured thermal conductivity λ_i

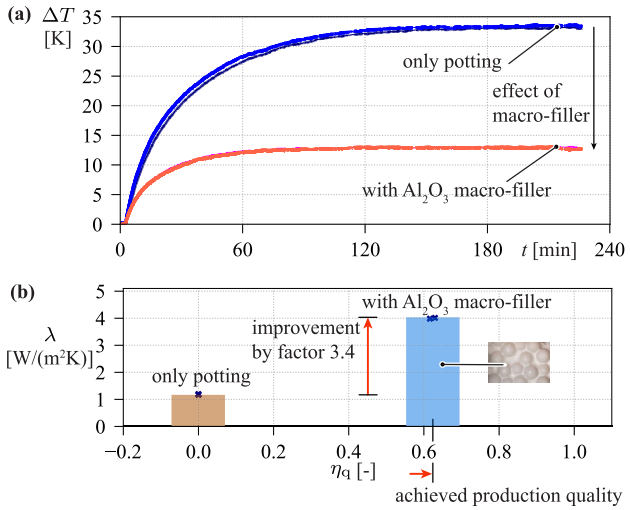

FIGURE 13. (a) Measured temperature difference rises in the thermal conductivity measurement units for only potting material and for the novel ceramics macro-filler composite (MAFC). (b) The measured increase in thermal conductivity of the ceramic macro-filler composite compared to the pure potting material by a factor of 3.4.

is relevant and results as:

$$\lambda_{c,i} = \frac{(Q_i - Q_{\text{leak,ins},i}) \cdot L_t}{A \cdot \Delta T_{\text{C-HS},i}}. \tag{20}$$

The resulting conductivities are shown in Fig. 13(b). The measured thermal conductivity for the pure potting with ER2074 of 1.18 W/(m · K) averaged over two units deviates only 5.6 % from the data sheet value of 1.25 W/(mK). This validates the experimental measurement procedure. The Al_2O_3 MAFC showed over two units an averaged thermal conductivity of $\lambda_c = 4.0\,\text{W/(mK)}$. The corresponding two paired conductivity measurements of the same material types coincide very well, as shown in Fig. 13(b). This indicates a good repeatability of the MAFC production method. The achieved production quality of $\eta_q > 0.6$ was determined by measuring the weight of the amount of macro-filler spheres filled. The measured improvement of the thermal conductivity by a factor of 3.4 validates experimentally the theoretically predicted excellent heat conduction capabilities of Al_2O_3 MAFC - while being electrically an insulator.

For the O-SBMs with $\eta_{\text{O-SBM}} = 89.2\,\%$, a peak continuous shaft power at 100 krpm of 280 W and a MAFC with a conductivity of 4 W/(m · K), the thermal resistance of the thermal bridge between winding and heatsink analytically calculated is 0.66 K/W. Therefore, the temperature drop from the stator winding to the heatsink is reduced to 22.4 K. For a heatsink temperature of 40°C, the winding surface temperature is reduced from 114.6°C with conventional potting to 62.4°C with MAFC. This temperature is acceptable for the close by position sensing electronics.

The solution S3 is therefore validated. Thus, in this article, a solution to the in literature known passive cooling problem of ultra high-speed toroidal wound slot-less motors is found, theoretically predicted and experimentally validated. Tab. 5 summarizes the main findings of solution S3.

TABLE 5. Solution S3: novel macro-filler composite thermal bridge material MAFC - main result.

S3: problem remedy	main results
increase in stator thermal bridge thermal conductivity	thermal conductivity increase compared to potting material by factor 3.4 to $\lambda_c = 4.0\,\text{W/mK}$ with novel MAFC material

III. COMPONENT C2: SL-PUCF ROTOR

A. TECHNOLOGY GAPS FOR THE COMPONENT REQUIREMENT RC; SEALLESS FLUID PATH

State of the art pharmaceutical PUCFs have several rotary seals. They have the functions of a) sealing the process chamber from the production facility against contamination in both directions, b) sealing against reduced pressure or near vacuum outside the rotor, c) sealing as a connection between the rotor and both feed and discharge pipes during filling and emptying. However, they pose a contamination risk, generate friction losses and are speed-limited to approx. 40 krpm [20].

1) PROBLEM P4: NO SEALS FOR FLUID GUIDANCE

For the SL-PUCF, the rotary seal is replaced by the hermetically enclosed wall of the process chamber. This eliminates the risk of contamination through the seal. However, the functions of the seals in terms of guiding the fluid flow between the rotor inlet/outlet and the rotor are more difficult to achieve.

2) SOLUTION S4: NOVEL PUCF ROTOR TOPOLOGY

The fluid topologies in this article should not be compared with the solutions for slow to medium-speed disk stack centrifuges as in [15]. The extremely high speeds of PUCFs require fluid guidance at the smallest possible radii and thus peripheral speeds. In today's PUCFs, the rotor can be filled from below while stationary due to the rotary seals, shown in Fig. 14(a1). The rotor is accelerated after.

In a sealless concept, the fluid feed must come from above to prevent leaking. Proposed possible rotor topologies that allow the fluid to be automatically discharged from the rotor are shown in Fig. 14(a). Possible topologies are a discharge pipe from above, Fig. 14(a2), or a rotor with an integrated outlet valve, Fig. 14(a3), or a rotor with a bottom outlet, whereby a novel feature, an inflow distributor, ensures that dynamic filling from above is possible without the fluid falling through the rotor while rotating, Fig. 14(a4).

For sequential operation, i.e. repeated filling, separation and discharge, the topologies in Fig. 14(a2) and Fig. 14(a3) appear to be promising candidates, as slow, controlled filling and unloading is possible at standstill. However, the long thin feed tube is critical in terms of vibration, and for the topology in Fig. 14(a3), the rotor integrated valve adds complexity. However, these two topologies do not appear to be very advantageous for continuous feed separation

TABLE 6. Solution S4: novel PUCF rotor topology.

S4: problem remedy	main results
SL-PUCF rotor topology without seals for fluid guidance	novel SL-PUCF rotor topology without rotary seals, filled from the top dynamically while the rotor rotates, incorporating an inflow distributor to avoid fluid from falling through the rotor and leaking out

TABLE 7. Solution S5a: novel inflow distributor.

S5a: problem remedy	main results
novel inflow distributor which prevents fluid from falling through the rotor during dynamic filling	novel inflow distributor, with bores allowing for all radial positions fluid to enter the rotor; anisotropic fluid resistance in radial and axial direction enables fluid to fill radially inwards without falling through

and discharge. However, the novel topology of Fig. 14(a4) appears to be very suitable for this purpose and is therefore realized. It also appears attractive due to its robust and simple design.

Fig. 14(b) shows the operating states of the proposed SL-PUCF. Fig. 14(b1) shows the filling. The rotor is filled in contrary to the state of the art from above while the rotor spins, instead of at standstill from below. A novel inflow distributor prevents the liquid form falling through. Accordingly, the rotor fills radially inward, shown in Fig. 14(b2). Depending on the wanted ultracentrifugation process, the suspension is sedimented down to the rotor wall, or banded as shown in Fig. 14(b3). Examples of potential ways of extracting the separated suspension are: adding more of the cushion layer density gradient medium which forces radially the separated media inward, as shown in Fig. 14(b4) - or in an enrichment process constantly letting suspension entering and supernatant exiting, or as shown in Fig. 14(b5) reducing the rotational speed to gradually empty the rotor, or in case of an internal rotor valve of Fig. 14(b5), decelerating the rotor to standstill and releasing the banded media. Tab. 6 summarizes the main findings of solution S4.

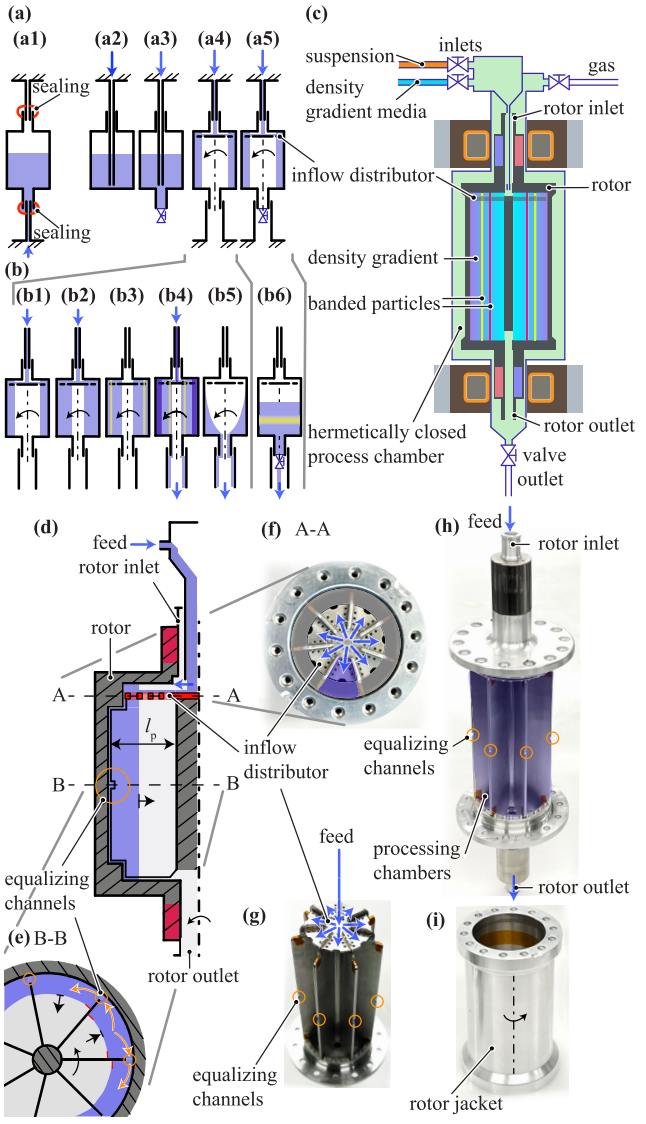

FIGURE 14. (a) PUCF rotor topologies, (b) operating states of the selected novel SL-PUCF rotor topology, (c) novel SL-PUCF concept, (d) rotor section view showing the novel inflow distributor and the novel fil-level equalizing channels, (e) section view of the equalizing channels, (f) hardware realization of the inflow distributor, and (g) of the equalizing channels, (h) assembled rotor fluid path, (i) rotor jacket.

3) PROBLEM P5: DYNAMIC FILLING

A challenge of the novel SL-PUCF rotor lies in filling while rotating, avoiding rotor unbalance. Given that the rotors of topologies in Fig. 14(a2) and and Fig. 14(a3) are operated only when completely filled, their magnetic suspension does not appear to be critical during operation. In contrast to those, the novel topology (a4) requires dynamic filling. The problems to be solved are P5a); preventing the fluid from falling through the rotor directly during filling while still maintaining direct access for the added fluid to all radius positions in the rotor during continuous filling in separation mode, and P5b); avoidance of unbalance during the filling process.

4) SOLUTION S5a: NOVEL INFLOW DISTRIBUTOR

Fig. 14(c) shows the layout of the proposed SL-PUCF. Fig. 14(d) shows a rotor section view thereof. The novel inflow distributor enables filling from the top while spinning. Small bores in axial direction allow the fluid to enter the rotor on all radii. But their small size results in the fluid flowing mainly radially outwards first, as it is the path of lowest resistance. Hence the inflow distributors anisotropic fluid resistance in radial and axial direction are the key factors. The bores through the inflow distributor Fig. 14(f) are placed, such that on all radii there is always an axial path available for the feed suspension. This avoids, that part of the feed suspension with a certain density is blocked

from axially entering the rotor. The radial path length l_p is a process parameter, which is adapted depending on the ultracentrifugation task. For the function of the inflow distributor, the larger l_p, the more difficult to maintain its function. Therefore the prototype in Fig. 14(f-g) was realized with the maximum l_p possible to investigate the worst case. Tab. 7 summarizes the main findings of solution S5a.

5) SOLUTION S5b: EQUALIZING CHANNELS

Novel equalizing channels between the divided rotor sectors enable unbalanced liquid in the rotor to equalize their level across the whole rotor and thus prevent unbalance. They are shown in Fig. 14(d,e,g,h). Fig. 14(h) shows the assembled SL-PUCF rotor, with its rotor jacket in Fig. 14(i). Tab. 8 summarizes the main findings of solution S5b.

TABLE 8. Solution S5b: novel equalizing channels.

S5b: problem remedy	main results
avoiding of rotor unbalance during filling	equalizing channels between divided rotor sectors let unbalanced liquid to level out, preventing rotor unbalance

IV. COMPONENT C3: BURST ARMOR

The rotational energy E_{rot} of the SL-PUCF rotor increases quadratically with the rotational speed Ω:

$$E_{rot} = \frac{1}{2} J_z \Omega^2 \tag{21}$$

with J_z being the moment of inertia. Thus, the energy of a single rotor at 100 krpm corresponds to that of 100 rotors at 10 krpm. This shows the fragment containment challenge associated with ultra-high speeds. The rotational energy stored in the rotor of the presented SL-PUCF prototype at 100 krpm is 10.2 kJ. This corresponds approximately to the muzzle energy of five 5.56 mm caliber assault rifle projectiles [21]. A PUCF needs accordingly a burst armor to retain rotor fragments in the event of the rotor bursting. This is also specified in the standard DIN EN 12547 [22].

A. TECHNOLOGY GAPS FOR THE COMPONENT REQUIREMENT RD; OPENABLE BURST ARMOR

As only one SL-PUCF prototype exists for this study, a destructive rotor burst containment validation test is not possible within the scope of this study. The standard DIN EN 12547 [22] does not provide any guidelines for the burst armor design either. To the knowledge of the author, no first principles based design guideline was published in literature for a PUCF burst armor. To asses its feasibility to successfully contain the rotor fragments, a simplified containment analysis is conducted.

As a first conservative assumption, it is assumed that the entire rotor energy must be absorbed by the openable burst armor (O-BA) in the form of plastic deformation to keep it contained. Energy dissipation due to e.g. friction losses and rotor deformation is conservatively omitted. The maximum absorbable deformation energy $E_{def,max}$ is calculated as the plastic deformation energy up to ultimate elongation ϵ_{us}, but conservatively without plastic hardening. The maximum achievable radial material stress is therefore conservatively assumed to be the yield stress $\sigma_{r,max} = R_{p0.2}$:

$$E_{def,max} = R_{p0.2} \cdot A_{BA} \cdot L_0 \cdot \epsilon_{us}, \tag{22}$$

where $A_{BA} = w_{BA} \cdot h_{BA}$ is the O-BA material cross-section area. The inner circumference of the armor is conservatively used as the initial length $L_0 = 2\pi r_{BA,i}$. For the alloy steel 1.7225 / 42CrMo4 ($R_{p0.2} = 550$ Mpa, $\epsilon_{us} = 0.14$, $R_m = 800$ Mpa [23]), this results in an absorbable deformation energy of the armor with a thickness of 2 cm of 20.7 kJ. This corresponds to a safety factor of $SF_{a,r} = 2$ of the burst armor against rupture. This shows the feasibility of the burst armor in general, not yet taking into account the opening joint weak points.

TABLE 9. Solution S6: joint load distribution.

S6: problem remedy	main results
new concept for removing joint weak points in the openable burst armor	multiple lugs distribute the joint load along the bolt, reducing the bolt shear stress, enabling a safety factor > 2 for approximated dimensioning

1) PROBLEM P6: JOINT WEAK POINTS

However, to be openable, a hinge and a corresponding locking mechanism must be designed, that are able to withstand the forces that occur. The load has to be transferred through the joints without resembling weak points as the source of failure.

2) SOLUTION S6: JOINT LOAD DISTRIBUTION

Fig. 15(a) shows the SL-PUCF prototype with O-BA. The maximum average circumferential force F_{BA} that occurs in the armor shown in Fig. 15(b) is conservatively:

$$F_{BA} = R_{p0.2} \cdot w_{BA} \cdot h_{BA}. \tag{23}$$

This force has to be transmitted by the armor bolts shown in Fig. 15(c). Instead of subjecting the load to only one bolt cross-section which would be a weak point, N_L lugs are attached to the two O-BA halves, shown in Fig. 15(d). They distribute the load over $(2 \cdot N_L - 1)$ bolt cross-sections. Neglecting bending of the bolt, the corresponding shear stress $\tau_{b,N}$ in the bolt cross-section A_b is

$$\tau_{b,N} = \frac{R_m \cdot w_{BA} \cdot h_{BA}}{A_b \cdot (2 \cdot N_L - 1)}. \tag{24}$$

The resulting shear stresses are shown in Fig. 15(e). The safety factor against bolt rupture $SF_{b,r}$ results as:

$$SF_{b,r} = \frac{\tau_{sB}}{\tau_{b,N}} = \frac{f_t \cdot R_m}{\tau_{b,N}} = \frac{f_t \cdot A_b \cdot (2 \cdot N_L - 1)}{w_{BA} \cdot h_{BA}} \cdot SF_{a,r}. \tag{25}$$

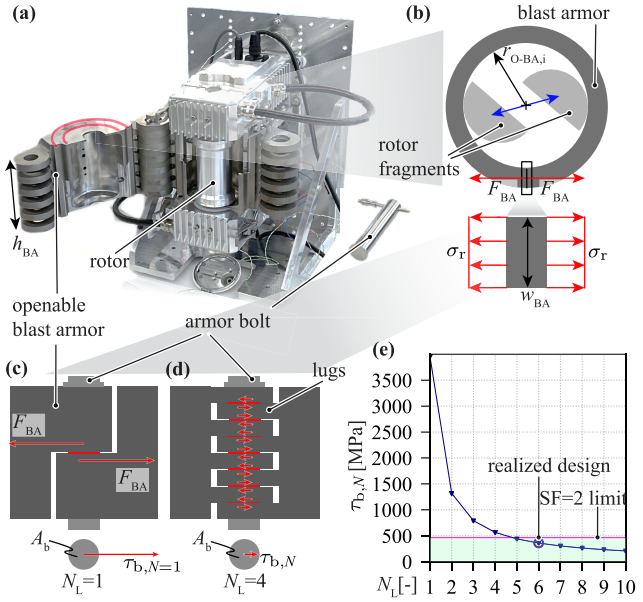

FIGURE 15. (a) SL-PUCF prototype with novel openable rotor burst armor (O-BA) with joints. (b) Simplified model for occurring circumferential stress within the armor while containing a rotor burst. (c) Load transfer at the joint with one lug would result in high bolt shear load. (d) Multiple lugs reduce the stress level on the bolt with load distribution along the bolt. (e) Stress reduction in the bolt depending on number of lugs.

The factor $f_t = \frac{\tau_{sB}}{R_m} = 0.58$ from [24] accounts for the reduced ultimate shear strength compared to the ultimate tensile strength of steel. $N = 1$, as in Fig. 15(c), would result in too thick and heavy bolts for a hinge. With $N = 6$, as realized in the prototype Fig. 15(a), the safety factor SF = 2 can be maintained for a bolt diameter of 2 cm.

The realized O-BA furthermore covers the rotor end faces, to prevent fragments from escaping axially. At the separating interface, the inner surface is designed to overlap to avoid fragments from escaping in between. The two armor halves are additionally designed such, that they are of identical geometry but still fit together.

The presented solution is scalable in length for longer rotors without change in the safety factor.

Tab. 9 summarizes the main findings of solution S6.

V. VALIDATION OF NOVEL SL-PUCF SYSTEM: SEDIMENTATION OF WHEY PROTEINS AS TEST-MEDIUM

The novel SL-PUCF concept is realized as a prototype. The SL-PUCF prototype was installed on a mobile laboratory unit together with the subsystems required for test operation, such as the mixing tank and feed pump, as shown in Fig. 16(a). The SL-PUCF rotor was successfully accelerated across the axial resonance frequency to 2 krpm, validating Solution S1 and S2. Particles and water were mixed in the mixing tank and then fed to the SL-PUCF by a magnetically levitated feed pump (Levitronix PuraLev i30SU). Whey proteins are used as test particles, mixed in water with 20 g/L. Their harmless nature, smaller size than viruses, very low cost and great availability as common food supplement, render them as a very attractive test medium for general working principle validation.

TABLE 10. SL-PUCF: system validation.

problem remedy	main results
passing of axial resonance frequency	successful, without rotor-housing contact
dynamic filling without fluid falling through rotor	successful
dynamic filling without destabilizing rotor unbalance	successful, stable suspension while filling
successful, stable high speed operation	20 krpm reached with filled rotor
rotor topology enables separation of particles	successful sedimentation of whey proteins at 20 krpm
operation without excessive winding surface temperature with passive cooling	successful, SL-PUCF operation at 20 krpm with winding surface temperature of 40.8° C

Using the O-SBMs magnetic bearing functionality as a sensor makes it possible to monitor the SL-PUCF dynamic rotor filling process by measuring the SL-PUCF rotor weight, shown in Fig. 16(b). It shows the rotor weight increase determined via the axial rotor position measurement during the dynamic filling of the SL-PUCF rotor at 2 krpm. It shows a constant feed rate, controlled by Levitronix Flow Control with the feed pump together with a inline Levitronix ultrasonic flow sensor. This validates experimentally, that the contact-less dynamic filling of the SL-PUCF rotor during stable levitated rotation from above via the inflow distributor works. This validates solutions S4-S5. After successfully filling of the SL-PUCF rotor, it was accelerated successfully stably suspended to 20 krpm.

Sedimentation was conducted as a first experimental validation of the basic functionality of the SL-PUCF rotor as a PUCF. The rotor was brought to 0 rpm, and inspected, as shown in Fig. 16(c). A layer of sedimented whey proteins was detected and therefore the separation successful. The basic separating function of the SL-PUCF has thus been experimentally validated.

The winding surface temperature of the O-SBM at 20 krpm was measured with only passive motor cooling to be 40.8° C, which confirms experimentally also during system operation the exceptionally good thermal properties of the novel MAFC for stator heat dissipation. Tab. 10 summarizes the main findings of the SL-PUCF system validation.

VI. OUTLOOK ON NOVEL FUTURE SMART CAPABILITIY POTENTIAL OF THE PROPOSED SL-PUCF CONCEPT

The following gives an outlook to new capabilities and benefits, that the new SL-PUCF concept can offer to the PUCF application. Three case studies are given, experimentally validating selected capabilities.

A. SENSING WITH O-SBMS AS SENSORS

Magnetic bearings can measure the radial and axial rotor position via their inherent function with position sensors. In literature, methods for contactless measurement of the rotor temperature via e.g. high frequency impedance mea-

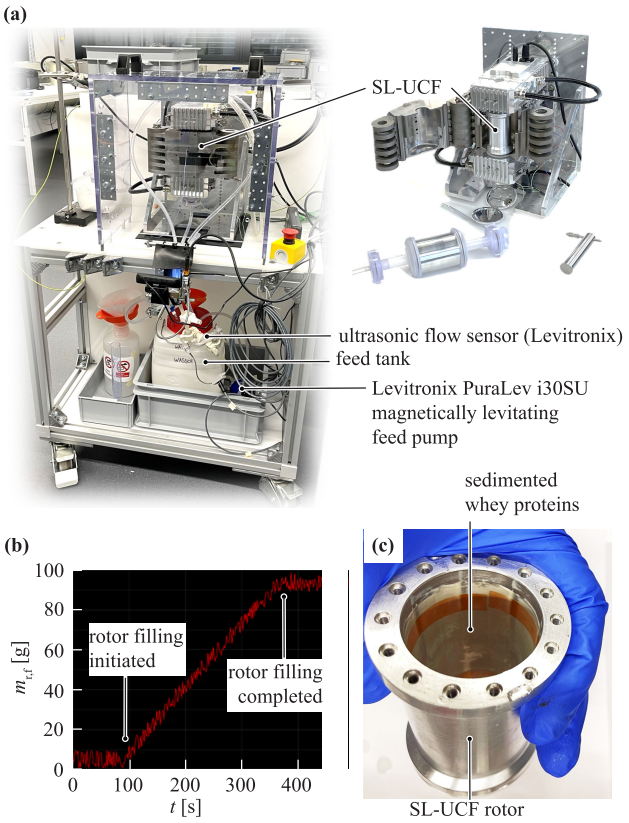

FIGURE 16. (a) Novel SL-PUCF prototype connected to mixing tank, feed pump, and feed flow sensor and a camera to observe the turbidity of the feed and the outflow of the SL-PUCF. (b) Measured fill-level of the SL-PUCF rotor by converted measurement of the axial (vertical) rotor position during filling, using the axial stiffness k_{ax} of the O-DSBMs. (c) First test for validating the fundamental function as a centrifuge: successfully sedimented whey proteins at 20 krpm on the rotor jacket wall.

surement of the magnetic circuit from the stator to the rotor are described in [25]. This means, that contactless monitoring of the PUCF rotor temperature is also conceivable in the future. This would help to monitor the rotor and therefore also rotor fluid temperature without contact.

Furthermore, information on the rotor, or the entire system structure can be obtained by measuring frequency responses through the magnetic bearing excitation, additionally extended by measuring the acoustic frequency response, as shown in [26].

B. SENSING: DESIGN VERIFICATION

The measurement of frequency responses can be used to verify the rotor dynamic properties of the rotor, including the bending resonance frequencies, to ensure that the rotor is sub-critical in the operating range. This is also possible during rotor rotation.

C. SENSING: HEALTH MONITORING

The presented measurable system properties are conceivable to be used for health monitoring in the future. For example, a scan of the rotor resonance frequencies at standstill, before the speed is increased, is conceivable. A scan of the acoustic frequency response, according to [26], to check the overall structure is also conceivable. Possible detectable system faults are, e.g., missing screws or cracks in the rotor that shift the rotor resonance frequencies out of a permissible tolerance band. It should even be possible to identify different rotor types in this way by measuring the frequency response of the magnetic bearing excitation and / or the rotor weight.

D. SENSING: CENTRIFUGATION PROCESS CONTROL

The Ultracentrifugation process control potentially benefits in the future from the newly measurable properties. The SL-PUCF rotor fill-level measurement during operation makes it possible to monitor the filling process and thus avoid overfilling the rotor. During centrifuging, for example, it is also conceivable to track the rotor weight increase during continuous feeding for enrichment. In principle, sedimented particles will also be registered as an increase in weight during standstill. The emptying of the rotor can also be monitored accordingly.

The detection of error states is also conceivable. Acoustic monitoring of the structure as in [26] can also be combined with acoustic monitoring of the hermetically sealed process chamber.

E. SMART CAPABILITY CASE STUDIES

1) O-SBMS AS SENSORS: FILL-LEVEL MEASUREMENT

The axial magnetic bearing stiffness can as demonstrated be used to measure changes in the rotor weight due to the resulting axial displacement. Knowing the density of the added suspension, the fill-level in the rotor can be measured during filling, discharging or during operation. This rotor mass measurement is shown in Fig. 16(b). The state of the completely filled rotor can be identified by the fact that the rotor weight does not increase any further during filling. Excess fluid exits directly at the rotor outlet. In principle, this even allows the density of the medium in the rotor to be determined, since the internal rotor volume is known.

2) DESIGN VERIFICATION: ROTOR BENDING RESONANCE MEASUREMENT

To measure the rotor bending resonance frequencies, the excitation was carried out as described in [26]. The direction of the excitation, i.e. forwards or backwards, can be freely selected. Here the excitation was carried out backwards. Thus the backward whirl mode was excited. The bending resonance frequencies were found to lie above 3 kHz. The rotor resonance frequencies lie with sufficient reserve outside the first-order excitation (sub-critical), which at 100 krpm lies at 1.667 kHz. The measurement of the rotor bending resonance frequencies during rotation at 2 krpm showed the typical lowering of the resonance frequencies for backward whirls with increasing speed. The first and second backward whirl bending resonance frequencies have decreased from

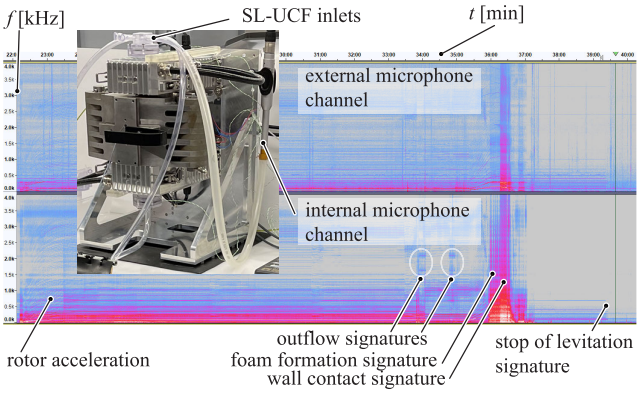

FIGURE 17. External and internal microphone recording spectrogram during a commissioning experiment with visible failure state signatures, showcasing the potential of acoustic process monitoring.

3.7 kHz to 3.65 kHz and 4.17 kHz to 4.13 kHz respectively, due to the increased speed. This verifies, that the backward whirl modes were excited, showcasing the capability to measure entire Campbell diagrams.

3) PROCESS CONTROL: ACOUSTIC PROCESS MONITORING

A microphone for process chamber monitoring is attached to the connections for process gas handling. This allows detection of fault conditions such as overfilling of the rotor, resulting in asynchronously rotating fluid in the process chamber, foam formation and rotor emptying. Fig. 17 shows exemplary the recorded channels of an external as well as an internal microphone which is connected to the inlets of the SL-PUCF during a commissioning experiments. Failure states like outflow of the rotor fluid, foam formation and wall contact, or stop of levitation leave distinct acoustic signatures. In the future, machine-learning based state recognition algorithms are conceivable.

VII. LIMITATIONS AND FUTURE IMPROVEMENTS

This section discusses limitations and future improvements of the main novel solutions found in this article.

A. SL-PUCF COMPONENT LEVEL SOLUTIONS

1) SOLUTION S1: YOKE INTERFACE SHOES

The proposed yoke interface shoes enable a RMS reduction of the axial stiffness ripple by 39% for a yoke air-gap surface increase of 33%. Their effect is limited to a reduction of the axial stiffness ripple to a tolerable level, but they cannot eliminate it completely.

As future improvements, larger reductions are conceivable with an even larger increase of the yoke air-gap surface, optionally also in axial direction. Furthermore, measures known from cogging torque reduction, e.g. forms of skewing, can in form of skewing of the yoke air-gap potentially further contribute to the ripple reduction.

Applications beyond the scope of this article of yoke interface shoes are any new developments of openable self-bearing motors or openable magnetic bearings.

2) SOLUTION S2: ROTOR MAGNET DESIGN

A guideline for optimal magnet orientation offset is proposed. As shown, the rotor magnet design remains a compromise between axial stiffness reduction, motor and magnetic bearing performance, mechanics and rotor dynamics. Furthermore, reasoning for the magnet length and position dimension selection is given. As a limitation, only a compromise is possible.

Improvements are mainly possible by improving the yoke interface shoes, while following the optimal magnet orientation guide.

The presented guideline and reasoning are applicable for any new system with two openable self-bearing motors or magnetic bearings with a common rotor.

3) SOLUTION S3: MACRO-FILLER COMPOSITE THERMAL BRIDGE MATERIAL

The MAFC material is validated to increase the thermal conductivity of potting material by a factor of 3.4 to 4 W/mK, which results in a massive reduction in temperature of critical components. Limitations are the cost of a more complex manufacturing process and the minimal gap size due to the macro-filler particle dimensions. The increase in manufacturing complexity is justified for application, where the benefit of the temperature reduction while avoiding eddy current losses is critical.

For future improvement, a mixture of different size MAFC filler particles to increase the theoretical limit of the MAFC packing density is suggested. However, it is a trade-off between thermal conductivity and high enough liquid characteristics which enable good surface contact.

Due to the MAFC particle dependent minimal gap size, MAFC is suited especially for applications with a large gap size or large volumes to be filled. Examples without limitation are electric machines, motors, self-bearing motors, magnetic bearings, motor windings or end-windings and magnetics in power electronics.

4) SOLUTION S4: SL-PUCF ROTOR TOPOLOGY

The proposed SL-PUCF rotor topology is validated for the principal separation function by successful sedimentation of whey proteins. Its design is currently limited to dynamic filling and unloading during rotor rotation.

Future extension of the topology in Fig. 14(a4) with a rotor-integrated valve as shown in Fig. 14(a5) can additionally simplify the unloading process. The rotor can then be emptied slowly and in a controlled manner at standstill. The valve could conceivably be activated by centrifugal force, mechanically from below or (electro-) magnetically.

The proposed SL-PUCF topology is generally applicable to any sort of centrifugation or ultracentrifugation application, however, the process for each application needs to be validated individually.

5) SOLUTION S5a: INFLOW DISTRIBUTOR

The inflow distributor is validated in its function to prevent fluid from falling through the rotor during filling. However, the flow details at the inflow distributor during filling are unknown.

Future studies can investigate the detailed inflow distributor flow field to find optimization potential.

The inflow distributor can be interesting for any top filled bowel centrifuge.

6) SOLUTION S5b: EQUALIZING CHANNELS

The SL-PUCF rotor with equalizing channels enabled validated stable dynamic filling during rotation. It should be investigated in future studies, if they lead to unwanted mixing, disturbing the separation process, or if they have no negative impact.

In case this should be discovered in future studies to be an issue, their distribution, size, and shape can be subjected to an optimization. Generally, the concept of equalizing channels can be of interest in any application with a rotor containing rotating fluid, especially for self-bearing motor or magnetic bearing suspended rotors.

7) SOLUTION S6: JOINT LOAD DISTRIBUTION

The newly derived approximate dimensioning of the novel openable burst armor showed a safety factor above two against rupture. Within this study, no rotor was accelerated until rotor burst, as the only prototype available should not be risked. In a future study, destructive burst tests with a rotational speed margin above the maximum rotor speed has to be conducted. The openable burst armor concept is generally applicable to any rotating machinery with needed rotor exchange or access and very high rotational energy to be contained.

B. SL-PUCF SYSTEM

1) EXPANDING OPERATING ENVELOPE

The proposed SL-PUCF is validated in its functionality. It is operated within this study at 20 krpm, to not risk destructive damage on this first prototype. In the precedent study [1], the first generation O-SBMs without the improvements of this study suspending horizontally instead of vertically a thin solid test-rotor, reached 103 krpm. The improved second generation of O-SBMs of this study therefore is highly likely to reach 100 krpm successfully also with a vertical rotor.

In a future study with more than one prototype available, the operating envelope will be successively expanded to higher rotational speeds. A vacuum system will be attached to lower the air pressure during high speeds to reduce rotor gas friction losses. A cooling system is foreseen around the process chamber to control the temperature of the rotor including its biotech payload. The full speed and power testing will also show the MAFCs performance under full load. However, the motor internal linearity of heat conduction with respect to the thermal resistance R_{Th} and the heat flux Q, $\Delta T = R_{\mathrm{Th}} \cdot Q$, combined with the MAFC thermal conductivity measurement and the very low winding surface temperature measurement result at 20 krpm, leads to the expectation of a very good thermal performance at 100 krpm as predicted.

2) APPLICATION SPECIFIC DEVELOPMENT

The SL-PUCF functionality was validated with the sedimentation of whey proteins.

In a future study, the SL-PUCF rotor will be investigated and optimized further for the viral nanotechnology application. Application development for new biotech devices is extensive and requires further studies, focusing on this. The SL-PUCF offers many application specific optimization parameters, such as the radial path length, application of density gradients and process related modes, e.g. filling and unloading speeds, processing times and profiles. Once the application protocols are established and validated, the up-scaling of the LaS-PUCF prototype to PiS-PUCF and PrS-PUCF can be conducted.

The proposed SL-PUCF is generally unlimited to any biopharmaceutical and other purification applications or to potential specialized applications even in clarification or other separation needs.

VIII. CONCLUSION

A novel sealless production ultracentrifuge type with two openable double self-bearing motors with novel features, tailored to vertically suspend its novel sealless rotor shielded by a novel openable burst armor was proposed and realized as a prototype. The current limitations of the state of the art of production ultracentrifuges for the manufacturing of viral vectors for gene therapies and vaccines were identified, system and component level requirements derived, component level problems identified, solutions presented and experimentally validated. This includes novel yoke interface shoes for openable self-bearing motor yokes, a guide to find optimal magnet alignment combinations and magnet dimensions for vertical rotor axis operation of such a system, the overcoming of axial bearing resonance, a novel scalable electrically insulating but highly thermally conductive macro-filler thermal bridge material for toroidal slotless ultra high-speed motors, a novel sealless flowpath design including a novel inflow distributor and equalizing channels and a novel openable ultracentrifuge burst armor. The general working principle of the novel sealless ultracentrifuge is validated experimentally by the successful sedimentation of whey proteins. Furthermore, an outlook is given to novel future capabilities for monitoring and process control thanks to the smart capabilities of the openable self-bearing motors and

examples are experimentally demonstrated in the form of case studies.

The development trend for production ultracentrifuges stagnated. This article identified limitations of the state of the art and proposes solutions. The research described in this article aims at bringing ultracentrifuges ''back in the game'' for future purification in viral nanotechnology, especially the separation of empty and full capsids.

The findings for the openable self-bearing motors to reduce the yoke air-gap influence can be used in any new application for openable self-bearing motors. The novel macro-filler composite thermal bridge material with an increased thermal conductivity by a factor of 3.4 compared to potting material can be of use for electric machines of any type in general to lower its (end-) winding temperatures or to increase power density.

ACKNOWLEDGMENT

The authors are greatly indebted to Levitronix GmbH for their scientific and technical contributions. They would like to thank Hanspeter Hubmann-Graf for the manufacturing of the copper heat-spreaders of the thermal conductivity measurement units.

REFERENCES

[1] E. J. Hubmann, R. Eberhard, C. F. Blaser, S. Erismann, D. Steinert, T. Nussbaumer, and J. W. Kolar, ''Magnetically self-bearing drive system for ultracentrifugation: Towards 100'000 rpm and 200'000 g,'' *IEEE Trans. Ind. Appl.*, vol. 60, no. 1, pp. 321–331, Sep. 2023, doi: 10.1109/TIA.2023.3314016.

[2] S. Wang, B. Liang, W. Wang, L. Li, N. Feng, Y. Zhao, T. Wang, F. Yan, S. Yang, and X. Xia, ''Viral vectored vaccines: Design, development, preventive and therapeutic applications in human diseases,'' *Signal Transduction Targeted Therapy*, vol. 8, no. 1, p. 149, Apr. 2023, doi: 10.1038/s41392-023-01408-5.

[3] J. T. Bulcha, Y. Wang, H. Ma, P. W. L. Tai, and G. Gao, ''Viral vector platforms within the gene therapy landscape,'' *Signal Transduction Targeted Therapy*, vol. 6, no. 1, pp. 1–24, Feb. 2021, doi: 10.1038/s41392-021-00487-6.

[4] U. Bezeljak, ''Cancer gene therapy goes viral: Viral vector platforms come of age,'' *Radiol. Oncol.*, vol. 56, no. 1, pp. 1–13, Feb. 2022, doi: 10.2478/raon-2022-0002.

[5] M. M. Segura, A. A. Kamen, and A. Garnier, ''Overview of current scalable methods for purification of viral vectors,'' in *Viral Vectors Gene Therapy*, 1st ed., Totowa, NJ, USA: Humana Press, 2019, ch. 4, pp. 89–116. [Online]. Available: https://link.springer.com/book/10.1007/978-1-61779-095-9

[6] Alfa Wassermann Inc. (2019). *Products Overview Continuous Flow Ultracentrifugation*. Accessed: Mar. 26, 2024. [Online]. Available: https://www.awst.com/cw/pdf/products/Overview/AWSTProductsOverviewv1.1.pd

[7] A. Flegler, M. Schneider, J. Prieschl, R. Stevens, T. Vinnay, and K. Mandel, ''Continuous flow synthesis and cleaning of nano layered double hydroxides and the potential of the route to adjust round or platelet nanoparticle morphology,'' *RSC Adv.*, vol. 6, no. 62, pp. 57236–57244, Jun. 2016, doi: 10.1039/c6ra09553d.

[8] M. Konrath, J. Gorenflo, N. Hübner, and H. Nirschl, ''Application of magnetic bearing technology in high-speed centrifugation,'' *Chem. Eng. Sci.*, vol. 147, pp. 65–73, Jun. 2016, doi: 10.1016/j.ces.2016.03.025.

[9] A. P. Gooders, N. L. Webb, G. J. Allen, and B. M. Richards, ''Total containment of a continuous-flow zonal centrifuge,'' *Biotechnol. Bioeng.*, vol. 23, no. 1, pp. 27549–27559, Jan. 1981, doi: 10.1002/bit.260230102.

[10] A. L. Gimpel, G. Katsikis, S. Sha, A. J. Maloney, M. S. Hong, T. N. T. Nguyen, J. Wolfrum, S. L. Springs, A. J. Sinskey, S. R. Manalis, P. W. Barone, and R. D. Braatz, ''Analytical methods for process and product characterization of recombinant adeno-associated virus-based gene therapies,'' *Mol. Therapy-Methods Clin. Develop.*, vol. 20, pp. 740–754, Mar. 2021, doi: 10.1016/j.omtm.2021.02.010.

[11] N. Singh and C. L. Heldt, ''Challenges in downstream purification of gene therapy viral vectors,'' *Current Opinion Chem. Eng.*, vol. 35, Mar. 2022, Art. no. 100780, doi: 10.1016/j.coche.2021.100780.

[12] A. Srivastava, K. M. G. Mallela, N. Deorkar, and G. Brophy, ''Manufacturing challenges and rational formulation development for AAV viral vectors,'' *J. Pharmaceutical Sci.*, vol. 110, no. 7, pp. 2609–2624, Jul. 2021, doi: 10.1016/j.xphs.2021.03.024.

[13] M. Wada, N. Uchida, G. Posadas-Herrera, H. Hayashita-Kinoh, Y. Tsunekawa, Y. Hirai, and T. Okada, ''Large-scale purification of functional AAV particles packaging the full genome using short-term ultracentrifugation with a zonal rotor,'' *Gene Therapy*, vol. 30, nos. 7–8, pp. 641–648, Mar. 2023, doi: 10.1038/s41434-023-00398-x.

[14] H. Agarwal, C. Thwin, and B. T. Kumaar, ''Single-use centrifugal separator enables intensification of the clarification process in biomanufacturing of recombinant proteins,'' *J. Chem. Technol. Biotechnol.*, vol. 98, no. 5, pp. 1321–1332, May 2023, doi: 10.1002/jctb.7351.

[15] J. Walker, Y. Lam, A. Loman, J. P. Smelko, and M. Rohr, ''Evaluation of a single-use disk stack centrifuge for improved efficiency and sustainability at 1000 L GMP manufacturing scale,'' *Biotechnol. Bioeng.*, vol. 120, no. 11, pp. 3347–3356, Nov. 2023, doi: 10.1002/bit.28519.

[16] A. Borisavljevic, *Limits, Modeling and Design of High-Speed Permanent Magnet Machines*, 1st ed., Berlin, Germany: Springer, 2012, doi: 10.1007/978-3-642-33457-3. [Online]. Available: https://link.springer.com/book/10.1007/978-3-642-33457-3

[17] A. Borisavljevic, S. Jumayev, and E. Lomonova, ''Toroidally-wound permanent magnet machines in high-speed applications,'' in *Proc. Int. Conf. Electr. Mach. (ICEM)*, Sep. 2014, pp. 2588–2593, doi: 10.1109/ICELMACH.2014.6960552.

[18] F. Ferrucci, M. Merdzan, F. G. Capponi, and E. Lomonova, ''Evaluation of eddy current losses in the cooling sleeve of a toroidal high speed permanent magnet machine,'' in *Proc. 2nd Global Power, Energy Commun. Conf. (GPECOM)*, Oct. 2020, pp. 125–130, doi: 10.1109/GPECOM49333.2020.9248718.

[19] H. Cohn, ''A conceptual breakthrough in sphere packing,'' *Notices Amer. Math. Soc.*, vol. 64, no. 2, pp. 102–115, Feb. 2017, doi: 10.1090/noti1474.

[20] N. G. Anderson, D. A. Waters, C. E. Nunley, R. F. Gibson, R. M. Schilling, E. C. Denny, G. B. Cline, E. F. Babelay, and T. E. Perardi, ''K-series centrifuges I. Development of the K-II continuous-sample-flow-with-banding centrifuge system for vaccine purification,'' *Anal. Biochemistry*, vol. 32, no. 3, pp. 460–494, Dec. 1969, doi: 10.1016/S0003-2697(69)80014-X.

[21] K. Piasta and P. Kupidura, ''Perspective armour-piercing intermediate cartridge projectile,'' *Problems Mechatronics Armament Aviation Saf. Eng.*, vol. 14, no. 1, pp. 89–104, Mar. 2023, doi: 10.5604/01.3001.0016.2961.

[22] *Zentrifugen—Allgemeine Sicherheitsanforderungen*, Standard DIN EN 12547, 2014.

[23] Thyssenkrupp Mater. Austria GmbH, Wien, Austria. *Werkstoffdatenblatt 34CrMo4 1.7220*. Accessed: May 2024. [Online]. Available: https://ucpcdn.thyssenkrupp.com/legacy/UCPthyssenkruppBAMXAustria/assets.files/download/baustahldatenblatt1.7220-1.7226.pdf

[24] H. Wittel, D. Jannasch, J. Vossiek, and C. Spura, *Roloff/Matek Maschinenelemente*, 24th ed., Wiesbaden, Germany: Springer, 2019, p. 996. [Online]. Available: https://link.springer.com/book/10.1007/978-3-658-26280-8

[25] L. He, Y. Feng, Y. Zhang, and B. Tong, ''Methods for temperature estimation and monitoring of permanent magnet: A technology review and future trends,'' *J. Brazilian Soc. Mech. Sci. Eng.*, vol. 46, no. 4, pp. 1–29, Mar. 2024, doi: 10.1007/s40430-024-04723-2.

[26] E. J. Hubmann, F. Weissofner, D. Steinert, T. Nussbaumer, and J. W. Kolar, ''Novel acoustic failure prediction method for active magnetic bearing systems,'' *IEEE/ASME Trans. Mechatronics*, vol. 29, no. 3, pp. 1181–1192, Apr. 2024, doi: 10.1109/TMECH.2023.3301815.

EMANUEL J. HUBMANN received the B.Sc. and M.Sc. degrees in mechanical engineering from the Swiss Federal Institute of Technology (ETH Zürich), Zürich, in 2016 and 2018, respectively, where he is currently pursuing the Ph.D. degree in advanced mechatronic systems and magnetic levitation with the Power Electronic Systems Laboratory (PES).

He was active in organizations such as J. Wagner AG; Swiss Armed Forces; Hitachi Zosen Inova AG; BRUSA Elektronik AG; Pediatric Heart Center, Department of Surgery, University Children's Hospital, Zürich; and Levitronix GmbH. His research focuses on the field of mechatronics, especially in electric drive systems and magnetic levitation for medical, biotech, and industrial applications.

Mr. Hubmann was a recipient of two IEEE conference prize paper awards and one poster award.

DANIEL STEINERT was born in Roth, Germany, in 1987. He received the M.Sc. degree in mechatronics from Dresden University of Technology, Dresden, Germany, in 2012, and the Ph.D. degree in bearingless motors from the Power Electronic Systems Laboratory, Swiss Federal Institute of Technology (ETH Zürich), Zürich, Switzerland, in 2015, where he worked on high-speed bearingless motors.

He is currently with Levitronix GmbH, Zürich, as the Head of the research group, where his research is focused on bearingless motor topologies, control concepts, losses, and applications of bearingless motors.

THOMAS NUSSBAUMER was born in Vienna, Austria, in 1975. He received the M.Sc. degree (Hons.) in electrical engineering from Vienna University of Technology, Vienna, in 2001, and the Ph.D. degree in power electronics from the Swiss Federal Institute of Technology (ETH Zürich), Zürich, Switzerland, in 2004. From 2001 to 2006, he was with the Power Electronic Systems Laboratory, ETH Zürich, where he was involved in research on modeling, design, and control of three-phase rectifiers; power factor correction techniques; and electromagnetic compatibility. Since 2006, he has been with Levitronix GmbH, Zürich, where he is currently involved as the Vice President of research and development on bearingless motors, magnetic levitation, and permanent-magnet motor drives for the semiconductor and biotechnology industry. His current research is focused on compact and high-performance mechatronic systems, including novel power electronics topologies, control techniques, drive systems, sensor technologies, electromagnetic interference, and thermal aspects.

JOHANN W. KOLAR (Life Fellow, IEEE) received the M.Sc. and Ph.D. degrees (summa cum laude-promotio sub auspiciis praesidentis rei publicae) from the University of Technology Vienna, Austria, in 1997 and 1999, respectively. Since 1984, he has been an Independent Researcher and an International Consultant in close collaboration with Vienna University of Technology in the fields of power electronics, industrial electronics, and high performance drive systems. He was appointed as an Associate Professor and the Head of the Power Electronic Systems Laboratory, Swiss Federal Institute of Technology (ETH), Zürich, in February 2001, and was promoted to a Full Professor, in 2004. He has proposed several novel converter concepts, including Vienna Rectifier, Sparse Matrix Converter, and the Swiss Rectifier. He has spearheaded the development of x-million rpm motors, and has pioneered fully automated multi-objective power electronics design procedures. He has personally supervised more than 90 Ph.D. students to completion, has published more than 1000 journal and conference papers and four book chapters, and has filed more than 200 patents in the course of international industry research collaborations. He has presented more than 40 educational seminars at leading international conferences. His current research interests include ultra-compact/efficient WBG converter systems, ANN-based design procedures, solid-state transformers, ultra-high speed drives, bearingless motors, and life cycle analysis of power electronics converter systems. He was elected to the U.S. National Academy of Engineering as an International Member, in 2021. He has received more than 40 IEEE TRANSACTIONS and conference prize paper awards, the 2014 IEEE Power Electronics Society R. David Middlebrook Achievement Award, the 2016 IEEE PEMC Council Award, the 2016 IEEE William E. Newell Power Electronics Award, the 2021 EPE Outstanding Achievement Award, and two ETH Zürich Golden Owl Awards for excellence in teaching. He has served as an IEEE PELS Distinguished Lecturer, from 2012 to 2016.